An update to this article is included at the end

Article

Cell Chemical Biology

Multiparatopic antibodies induce targeted downregulation of programmed death-ligand 1

Graphical abstract

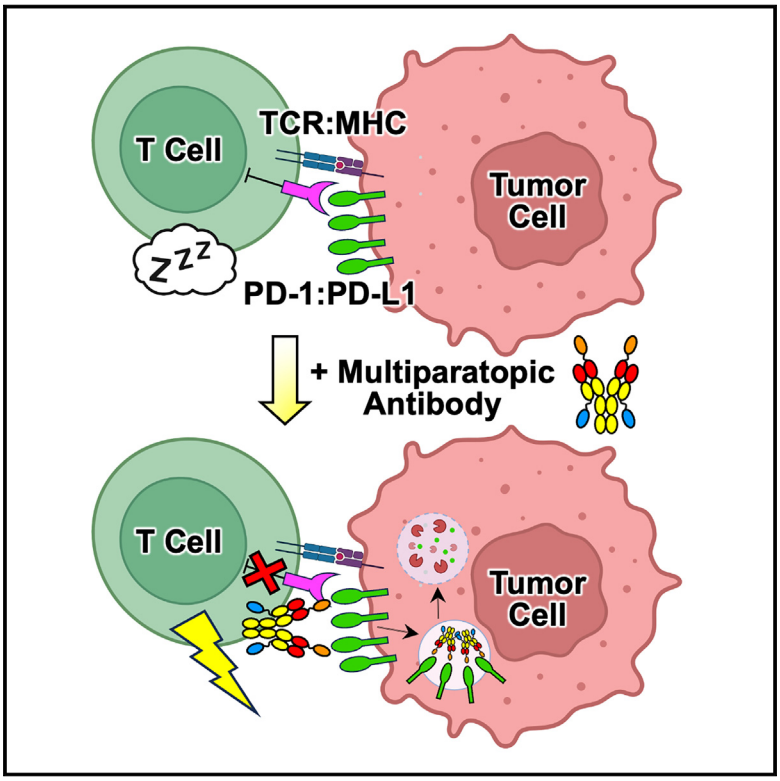

Authors

Seth D. Ludwig, Bunyarit Meksiriporn, Jiacheng Tan, ..., Helen M. Dooley, Sridhar Nimmagadda, Jamie B. Spangler

Correspondence

jamie.spangler@jhu.edu

In brief

Immune checkpoint proteins such as programmed death-ligand 1 (PD-L1) promote tumor progression and new approaches are needed to block signaling through these pathways. Ludwig et al. engineer anti-PD-L1 multispecific antibodies that induce downregulation of the target protein by engaging multiple epitopes on the ligand, synergistically reducing its immunosuppressive activities.

Highlights

- Discover panel of anti-PD-L1 antibody fragments that recognize unique epitopes
- Design multiparatopic antibodies that concurrently bind multiple sites on PD-L1
- Multiparatopic antibodies downregulate PD-L1 dependent on molecular properties
- Multiparatopic antibody-induced PD-L1 downregulation counteracts immunosuppression

Ludwig et al., 2024, Cell Chemical Biology *31*, 904–919
May 16, 2024 © 2024 Elsevier Ltd. All rights reserved.
https://doi.org/10.1016/j.chembiol.2024.02.014

CellPress

CellPress

Cell Chemical Biology

Article

Multiparatopic antibodies induce targeted downregulation of programmed death-ligand 1

Seth D. Ludwig,[1] Bunyarit Meksiriporn,[2,3,13] Jiacheng Tan,[2,13] Rakeeb Kureshi,[2] Akhilesh Mishra,[1,4] Kyle J. Kaeo,[1] Angela Zhu,[1] Georgia Stavrakis,[5] Stephen J. Lee,[1] David. J. Schodt,[6] Michael J. Wester,[6] Dhiraj Kumar,[1,4] Keith A. Lidke,[6] Andrea L. Cox,[7] Helen M. Dooley,[8] Sridhar Nimmagadda,[4,9] and Jamie B. Spangler[1,2,9,10,11,12,14,*]

[1]Department of Chemical and Biomolecular Engineering, Johns Hopkins University, Baltimore, MD 21218, USA
[2]Department of Biomedical Engineering, Johns Hopkins University School of Medicine, Baltimore, MD 21205, USA
[3]Department of Biology, School of Science, King Mongkut's Institute of Technology Ladkrabang, Bangkok 10520, Thailand
[4]Department of Radiology and Radiological Science, Johns Hopkins University School of Medicine, Baltimore, MD 21287, USA
[5]Department of Molecular Microbiology and Immunology, Johns Hopkins University School of Public Health, Baltimore, MD 21205, USA
[6]Department of Physics and Astronomy, University of New Mexico, Albuquerque, NM 87131, USA
[7]Department of Medicine, Johns Hopkins University School of Medicine, Baltimore, MD 21205, USA
[8]Department of Microbiology and Immunology, Institute of Marine and Environmental Technology (IMET), University of Maryland School of Medicine, Baltimore, MD 21201, USA
[9]Bloomberg~Kimmel Institute for Cancer Immunotherapy, Sidney Kimmel Comprehensive Cancer Center, Johns Hopkins University School of Medicine, Baltimore, MD 21231, USA
[10]Translational Tissue Engineering Center, Johns Hopkins University School of Medicine, Baltimore, MD 21231, USA
[11]Department of Oncology, Johns Hopkins University School of Medicine, Baltimore, MD 21205, USA
[12]Department of Ophthalmology, Wilmer Eye Institute, Johns Hopkins University School of Medicine, Baltimore, MD 21231, USA
[13]These authors contributed equally
[14]Lead contact
*Correspondence: jamie.spangler@jhu.edu
https://doi.org/10.1016/j.chembiol.2024.02.014

SUMMARY

Programmed death-ligand 1 (PD-L1) drives inhibition of antigen-specific T cell responses through engagement of its receptor programmed death-1 (PD-1) on activated T cells. Overexpression of these immune checkpoint proteins in the tumor microenvironment has motivated the design of targeted antibodies that disrupt this interaction. Despite clinical success of these antibodies, response rates remain low, necessitating novel approaches to enhance performance. Here, we report the development of antibody fusion proteins that block immune checkpoint pathways through a distinct mechanism targeting molecular trafficking. By engaging multiple receptor epitopes on PD-L1, our engineered multiparatopic antibodies induce rapid clustering, internalization, and degradation in an epitope- and topology-dependent manner. The complementary mechanisms of ligand blockade and receptor downregulation led to more durable immune cell activation and dramatically reduced PD-L1 availability in mouse tumors. Collectively, these multiparatopic antibodies offer mechanistic insight into immune checkpoint protein trafficking and how it may be manipulated to reprogram immune outcomes.

INTRODUCTION

Programmed death-ligand 1 (PD-L1) is a member of the B7 family of immunoregulatory ligands that play a pivotal role in regulation of the cellular and humoral immune responses. PD-L1 is expressed in both lymphoid and non-lymphoid tissue, where it is involved in suppression of immune activity through activation of the co-inhibitory receptor programmed death-1 (PD-1), which is expressed primarily on T cells, but also some natural killer (NK) cells and monocytes.[1–4] Immunosuppressive pathways (also called immune checkpoint pathways) such as the PD-1/PD-L1 axis are essential for maintaining healthy immune regulation. However, these pathways are frequently exploited by cancer cells and immune cells in the tumor microenvironment to evade immune recognition. Indeed, PD-L1 expression is observed in various forms of cancer, both constitutively and as a feedback response to inflammatory signals, resulting in inhibition of tumor-specific T cell responses.[5–9] To counteract this effect, monoclonal antibodies known as immune checkpoint inhibitors (ICIs) have been developed, which target immune checkpoint proteins such as PD-L1.[10,11] ICIs that disrupt the PD-1/PD-L1 interaction have shown unprecedented success in treating a variety of cancers, including 3 FDA-approved anti-PD-L1 antibodies: atezolizumab, durvalumab, and avelumab.[12–14] However, the immunological mechanisms by which anti-PD-L1 therapies function are complex and still only partially understood.

 © 2024 Elsevier Ltd. All rights reserved.

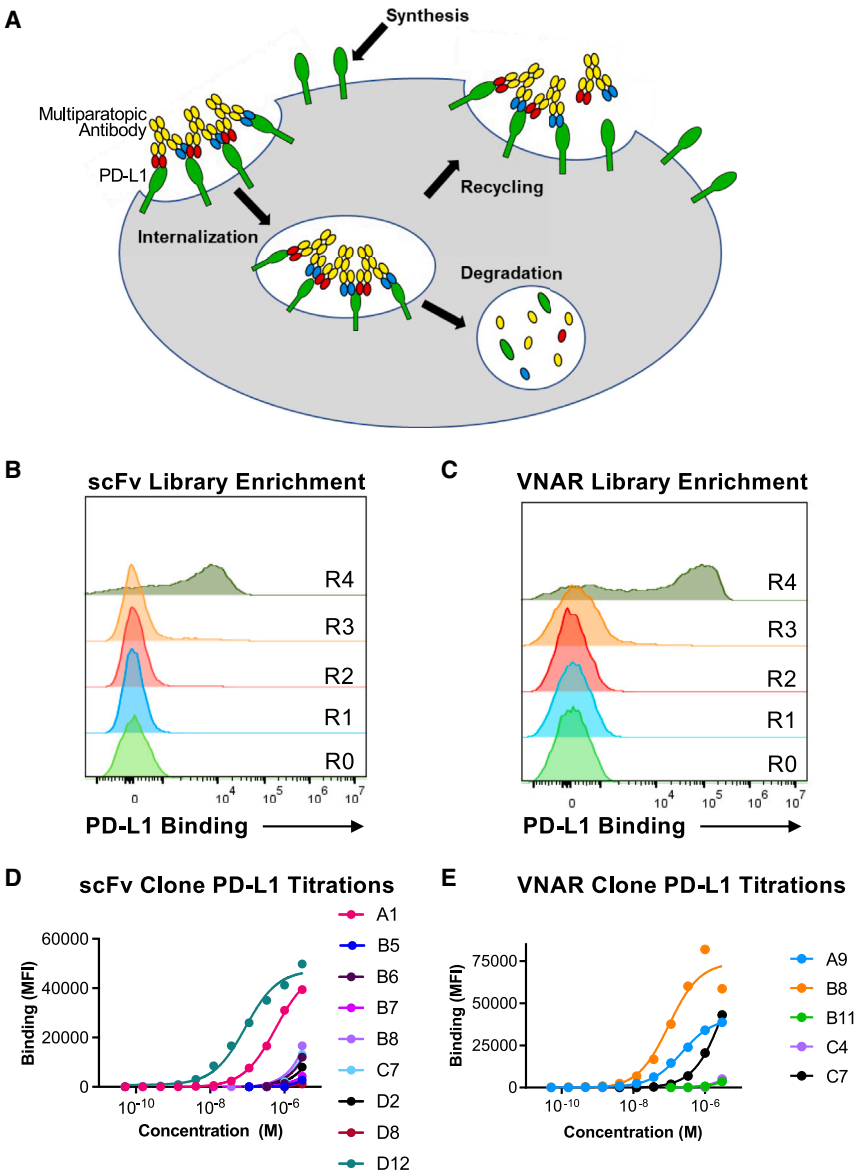

Figure 1. Discovery of PD-L1-targeted antibodies

(A) Schematic representation of receptor trafficking following treatment with a multiparatopic antibody that targets two non-competitive epitopes on PD-L1.

(B and C) Progression of PD-L1 binding (1,000 nM) over four rounds of selections against 2 yeast surface-displayed libraries: (B) a synthetic scFv library;[41] and (C) a VNAR library derived from immunization of sharks with the PD-L1 extracellular domain.

(D and E) On-yeast PD-L1 binding titrations of individual clones isolated from: (D) the synthetic scFv library; and (E) the immunization-derived VNAR library, as measured by flow cytometry analysis.

See also Figures S1 and S2, Tables S1 and S2.

Blockade of the PD-1/PD-L1 pathway has been shown to restore functionality to chronically exhausted $CD8^+$ T cells,[15] suggesting that tumor-associated PD-L1 primarily inhibits proliferation and effector functions of activated tumor-specific T cells. Upregulation of PD-L1 by tumor cells is often associated with adaptive resistance to endogenous tumor-specific immune responses, in particular the secretion of interferon-gamma (IFN-γ) as well as inflammatory cytokines.[9,16] But although high-level expression of PD-L1 in tumor biopsies has been generally used as a criterion to guide anti-PD-L1 treatment, it has become increasingly clear that PD-L1 expression on infiltrating immune cells, including myeloid cells and T cells can in many cases be sufficient to predict therapeutic efficacy.[14,17,18] Some data suggest that PD-L1 expression on antigen-presenting cells (APCs) may play a vital role in determining the efficacy of anti-PD-L1 therapy, whereas PD-L1 on tumor cells and tumor infiltrating lymphocytes is irrelevant, highlighting the continued uncertainty on the underlying mechanisms of PD-L1-targeted ICIs.[19] Recent data reporting the ability of PD-L1 to form ligand-ligand heterodimers with CD80, imply that PD-L1 may exert additional, and as of yet unclear, effects on the co-stimulatory CD28 pathway and the co-inhibitory cytotoxic T-lymphocyte associated protein 4 (CTLA-4) pathway.[20–22] Despite incomplete understanding of the immune effects of anti-PD-L1 antibodies, these drugs have been shown to achieve complete and durable cures in some patients, which has led to their approval across cancer types, including non-small cell lung cancer (NSCLC) and Merkel cell carcinoma.[13,14] Unfortunately, patient response rates to anti-PD-L1 therapies remain disappointingly low and most tumor regressions are only partial,[23–25] necessitating the development of new mechanistic strategies to enhance the efficacy of immune checkpoint protein-targeted therapies.

One potential approach to introducing alternative mechanisms for PD-L1-targeted therapies is through the development of antibodies that modulate the molecular trafficking dynamics of this protein. All 3 clinically approved anti-PD-L1 drugs act through a common mechanism that entails binding to PD-L1 and sterically blocking its interaction with the PD-1 receptor.[26,27] A potential complementary mechanism could involve targeting several distinct binding epitopes on PD-L1 with either a combination of antibodies or a single multispecific antibody (known as a multiparatopic antibody), in order to cross-link and subsequently internalize and degrade surface-expressed protein (Figure 1A). Antibody cocktails[28–30] and multiparatopic antibodies[31–38] have been previously reported to increase endocytosis and lysosomal degradation of a variety of surface proteins,

including the receptor tyrosine kinases epidermal growth factor receptor (EGFR), human epidermal growth factor receptor 2 (HER2), and MET, as well as major histocompatibility complex (MHC) class I molecules, transferrin receptor, and the glycosylphosphatidylinositol (GPI)-linked enzyme CD73. In the case of cancer-associated antigens, such as EGFR and HER2, downregulation induced by these antibody cocktails and multiparatopic antibodies has been shown to elicit robust antitumor activity.[28,32] Multiparatopic antibodies in particular have frequently been shown to increase therapeutic efficacy compared to both monoclonal antibody treatments and combinations of their constituent parent antibodies.[31–36] Recently, Park and colleagues demonstrated an effective immune checkpoint inhibition strategy based on small molecule-induced internalization of PD-L1,[39] and Zhang and colleagues reported antibodies that alter the immunostimulatory activities and toxicity of anti-CTLA-4 therapy through modulation of trafficking behavior,[40] offering promising rationale for exploring the trafficking dynamics of immune checkpoint proteins. Here, we sought to extend the concept of multiparatopic antibody-mediated downregulation to the PD-L1 system. We engineered bi- and tri-paratopic antibody fusion proteins based on the clinically approved drug atezolizumab and demonstrated that these molecules induced rapid clustering and internalization of PD-L1, leading to increased receptor degradation. We further showed that treatment with the most active PD-L1-targeted multiparatopic antibody resulted in improved immune cell activation and led to durable suppression of PD-L1 in mouse tumor models. Overall, our study establishes PD-L1-targeted multiparatopic antibodies as promising tools for interrogating and manipulating immune checkpoint protein pathways.

RESULTS

Discovery of PD-L1-targeted antibodies

To identify new PD-L1 binding proteins, we selected a naive yeast-displayed synthetic antibody single-chain variable fragment (scFv) library[41] against the extracellular domain (ECD) of PD-L1 by performing iterative rounds of magnetic-activated cell sorting (MACS) and fluorescence-activated cell sorting (FACS)[42,43] (Figure 1B). Several PD-L1-specific clones were identified from the enriched library, with affinities ranging from 10- to >1,000-fold weaker than atezolizumab (Figure 1C; Table S1). Additionally, we screened a yeast-displayed variable new antigen receptor (VNAR) library developed through immunization of nurse sharks with the PD-L1 ECD.[44] Successive rounds of MACS and FACS led to identification of additional PD-L1 binding domains, which also showed a range of affinities from 10- to >1,000-fold weaker than atezolizumab (Figures 1D and 1E; Table S1).

Newly discovered anti-PD-L1 antibodies target distinct epitopes compared to atezolizumab

Among the isolated clones from the enriched libraries, 1 scFv (D12) and 2 VNARs (A9 and B8) were expressed in soluble form as variable fragments through transient transfection of human embryonic kidney (HEK) 293F cells, alongside the scFv of atezolizumab. Bio-layer interferometry studies revealed that the equilibrium binding affinity (K_D) for PD-L1 was 5.3 nM for atezolizumab, compared to 100 nM for D12, 130 nM for A9, and 34 nM for B8 (Figure 2A; Table S1). We next sought to examine overlap between the PD-L1 binding epitopes of the various binders through bio-layer interferometry-based cross-competition studies. Whereas the scFv D12 was found to compete with atezolizumab for PD-L1 binding, both VNAR domains (A9 and B8) were found to be noncompetitive with atezolizumab (Figure 2B). A9 and B8 were further determined to be noncompetitive with D12 (Figure 2C), as well as with one another (Figure 2D), suggesting the presence of at least 3 unique binding epitopes among these clones. Upon examining competition of the various anti-PD-L1 binding domains with the PD-1 receptor, we found that both atezolizumab and D12 directly compete with PD-1 for PD-L1 engagement whereas B8 is noncompetitive with PD-1 (Figure S1A). Interestingly, the interplay between A9 and PD-1 was more nuanced, with simultaneous but slightly attenuated binding of PD-1 to PD-L1 observed in the presence of the VNAR domain, possibly due to allosteric effects. All three binding domains were found to not cross-react with mouse PD-L1, in contrast with atezolizumab which binds mouse PD-L1 albeit with a slightly lower affinity than human PD-L1 (Figure S1B). In the absence of crystallographic structures for D12, A9, and B8 in complex with PD-L1, we used high ambiguity driven protein-protein docking (HADDOCK, web server version 2.4)[45] to model the interactions of our newly discovered anti-PD-L1 binding domains with the target protein, and we compared the resulting structural predictions with the crystallographic structures of the atezolizumab/PD-L1[26] and PD-1/PD-L1[46] and complexes (Figures S1C and S1D). Interface residues of each protein complex were determined by the Proteins, Interfaces, Structures, and Assemblies (PISA) service at the European Bioinformatics Institute[47] and structural figures were visualized with PyMOL.[48] In line with competition studies (Figures 2A–2D) and PD-1 binding analysis (Figure S1A), the binding epitopes of scFvs atezolizumab and D12 on PD-L1 overlap extensively with the binding epitope of PD-1, and atezolizumab, D12, and PD-1 all bind on "top" of the PD-L1 molecule (see Figures S1C and S1D). In contrast, VNARs A9 and B8 were predicted to bind on different "sides" of the PD-L1 molecule, and the VNAR binding epitopes on PD-L1 did not overlap with the binding epitope of PD-1.

Engineered anti-PD-L1 multiparatopic antibodies downregulate PD-L1 surface expression on cancer cells

We utilized the 4 recombinantly expressed PD-L1-targeted proteins (scFvs atezolizumab and D12 and VNARs A9 and B8) to produce a panel of bi- and tri-paratopic antibody constructs. The variable fragments of D12, B8, and A9 were fused to the N- and C-termini of the heavy chain (HC) and/or light chain (LC) of the full-length atezolizumab human immunoglobulin G1 (IgG1) antibody using flexible $(Gly_4Ser)_3$ 15 amino acid linkers (except for the C-terminal LC constructs, which used a flexible $(Gly_4Ser)_2$ 10 amino acid linker). Additionally, heterodimeric antibody fusion proteins were produced using engineered knobs-into-holes mutations in the HC constant domain (Figure 2E).[49,50] To ensure proper chain pairing of asymmetric multiparatopic antibodies, a recently published method for single-chain Fab expression was utilized.[51] As in the parent atezolizumab antibody, the N297A mutation was included in the HC constant domain to reduce interactions with Fc gamma receptors

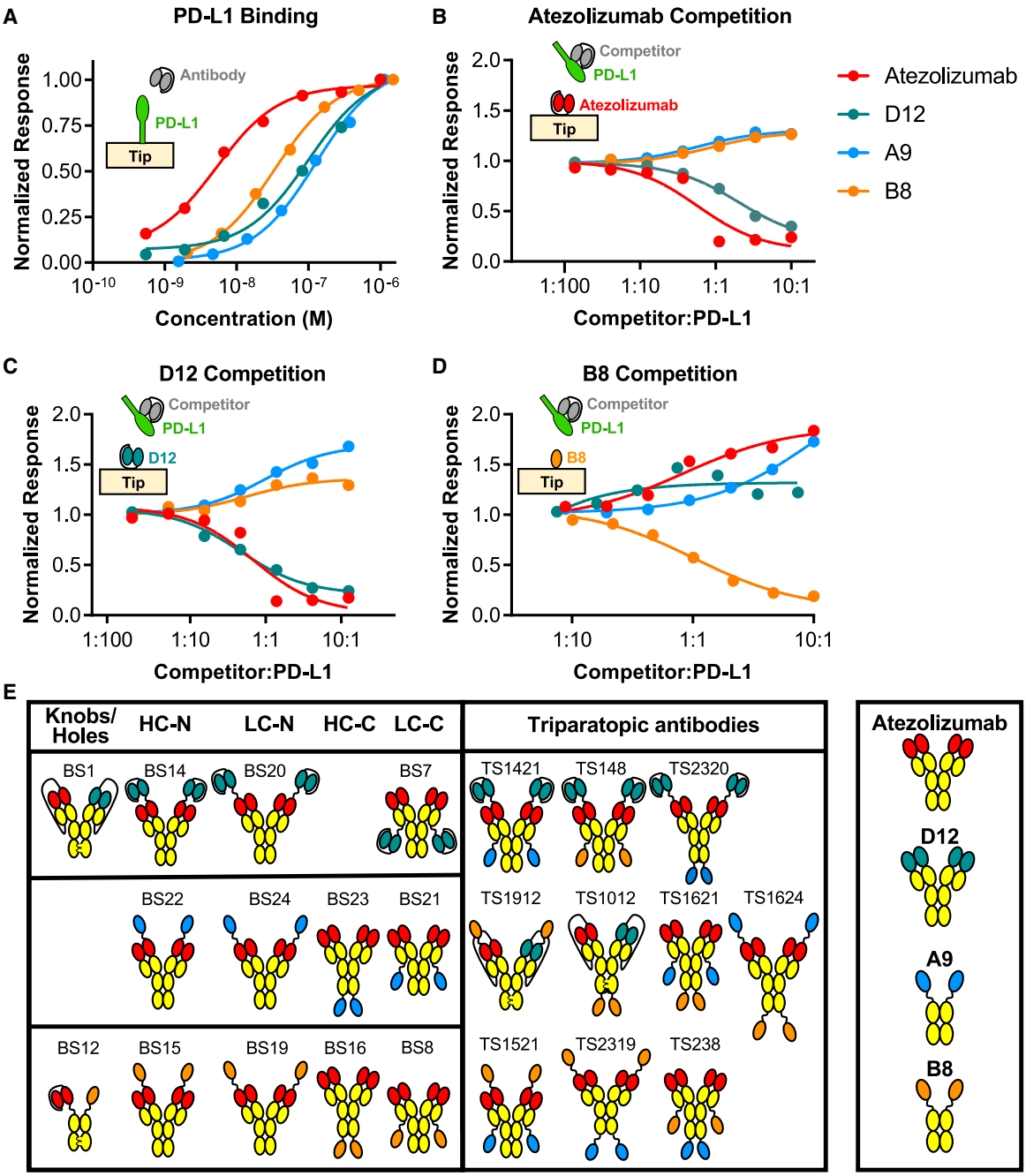

Figure 2. Design of multiparatopic antibodies targeting PD-L1

(A) Equilibrium binding titrations of two scFv (atezolizumab and D12) and two VNAR (B8 and A9) fragments against immobilized PD-L1, as measured by bio-layer interferometry.

(B–D) Cross-competition analysis of PD-L1 binding between two scFvs (atezolizumab and D12) and two VNARs (B8 and A9). Charts depict bio-layer interferometry analysis of equilibrium binding of an immobilized antibody fragment ((B) atezolizumab, (C) D12, and (D) B8) to saturating amounts of PD-L1 ((B and D) 100 nM, (C) 250 nM) in the presence of varying concentrations of the indicated soluble competitor.

(E) Schematic depictions of bi- and triparatopic antibody fusion proteins. All constructs are based on the atezolizumab human IgG1 antibody, and include either N or C terminal fusions to the heavy and/or light chains, or asymmetric knobs-into-holes Fc mutations.

See also Figures S1 and S2, and Table S2.

and thereby mitigate antibody-dependent destruction of PD-L1-expressing T cells.[52] Atezolizumab-based multispecific antibody fusion proteins were expressed via transient transfection of HEK 293F cells, and high purity was achieved for the various antibody constructs following separation by size-exclusion chromatography (Figure S2). To ensure that aggregates and/or multimers were removed from the protein preps, samples of atezolizumab and TS1521 were run over the size-exclusion column a second time (Figure S3A). A single monodisperse peak was observed in both cases, confirming that the samples which were used in all experiments were free of aggregates and multimers. Moreover, we found TS1521 to be robust to freeze-thaw and remarkably stable at physiological temperature over a period of 3 weeks (Figure S3B), providing a positive indication for developability.

Using MDA-MB-231 human triple negative breast cancer cells, we examined the ability of each of the engineered bi-/triparatopic constructs to downregulate PD-L1 expression (Figures 3A and 3B). After treatment with antibody for 14 h, surface PD-L1-bound antibody was stripped using an acidic solution (Figures S3C and S3D) prior to surface PD-L1 staining and detection by flow cytometry. The effectiveness of downregulation was observed to be affected by both the topology of the multiparatopic construct as well as the binding epitopes that were engaged. For example, in the context of biparatopic antibodies (Figure 3A), fusing B8 to the N-terminus of the HC (BS15) resulted in approximately 25% greater PD-L1 downregulation compared to fusion to the N-terminus of the LC (BS19), whereas A9 and D12 did show much variation between N-terminal HC or LC fusion orientations. Surprisingly, bivalent biparatopic antibodies (BS1 and BS12) could achieve equivalent downregulation to the tetravalent constructs, although the relative performances were also dependent on geometry. D12 fusions were the least effective on average, which was expected based on the overlapping binding epitopes between D12 and atezolizumab. A9 fusions were the most effective on average. B8 fusions varied most significantly with topology, and the B8 N-terminal HC construct (BS15) was found to be the most effective of all biparatopic antibodies that were tested.

Triparatopic antibodies were generally more efficient downregulators compared to their component biparatopic antibodies, though only a few of the triparatopic constructs were more effective than BS15 (Figure 3B). As with biparatopic antibodies, topology and epitope coverage were important determinants for downregulation extent. For instance, a triparatopic antibody with B8 N-terminally fused to the HC and A9 C-terminally fused to the LC (TS1521) elicited 28% greater downregulation than a similar antibody that relocated B8 to the C-terminus of the HC (TS1621) and 27% greater downregulation than another similar antibody that substituted D12 at the HC N-terminus (TS1421). Of note, only triparatopic antibodies that engaged 3 unique epitopes of PD-L1 (i.e., containing atezolizumab scFv and A9 and B8 VNARs) were found to be more effective than the most active biparatopic antibody (BS15). Among the triparatopic antibodies with 3 unique epitopes that were tested, geometries that positioned A9 at the C-terminus and B8 at the N-terminus were most effective at inducing PD-L1 downregulation. Overall, MDA-MB-231 downregulation studies identified the most actively downregulating anti-PD-L1 multiparatopic antibody in our panel to be TS1521, which decreased surface PD-L1 levels by 60–70%.

To assess the effects of target protein expression levels on multiparatopic antibody-mediated downregulation, we assessed antibody-induced PD-L1 downregulation on 5 different tumor cell lines, representing a spectrum of expression levels that would likely be found in human cancers, ranging from 5,800 to 526,000 copies per cell (Figure 4A). We observed that the extent of downregulation increases modestly with increasing PD-L1 expression up to a density of at least 526,000 copies per cell (Figures 4A and 4B). Very low receptor density (for instance on the A549 cell line) eliminated multiparatopic antibody-mediated PD-L1 downregulation effect entirely, which could be due to geometric challenges in cross-linking PD-L1 when few copies are present on the surface. A similar trend of downregulation dependence on PD-L1 surface density was observed for multiparatopic antibodies BS1, BS15, and TS2319 (Figures S4A and S4B). Interestingly, the threshold for PD-L1 surface density required to enable downregulation was found to vary with antibody design (Figures 4A, 4B, S4A, and S4B). For instance, the biparatopic antibody BS15 induced significant downregulation on cells that expressed >41,000 receptors/cell, whereas the triparatopic antibody TS2319 only induced significant downregulation on cells that expressed >347,000 receptors/cell. Treatment with a combination of the atezolizumab and D12 monoclonal antibodies did not induce downregulation of PD-L1 levels, whereas treatment with a biparatopic antibody incorporating both binding fragments (BS1) significantly reduced surface PD-L1, supporting an important role for combining multiple paratopes within a single molecule (Figure S4C). Downregulation was also found to be dependent on antibody concentration, with maximal reduction in PD-L1 surface levels observed at saturating concentrations of multiparatopic antibody (Figure S4D; Table S2). This result is consistent with a model in which surface cross-linking of PD-L1 precipitates downregulation. For the specific case of BS1, the effective concentration (EC_{50}) of the downregulation effect was found to be 0.40 nM, substantially more potent than the affinities of the individual antibody domains for PD-L1 (ranging from ≈5 to 130 nM). Taken together, the results of our downregulation assays establish that multiparatopic antibodies mediate robust downregulation of surface PD-L1 across cancer cell lines in a manner that is dependent on antibody topology, epitope engagement, and surface protein density.

Multiparatopic antibodies induce PD-L1 internalization, clustering, and lysosomal sorting

We next sought to understand the receptor trafficking patterns that underlie the downregulating effects of engineered multiparatopic antibodies. Kinetic studies with TS1521 on H2444 human NSCLC cells showed that antibody-induced downregulation occurs rapidly upon addition of the treatment, reaching steady state within 4–6 h (Figure 4C). In contrast, the parent monoclonal antibody (atezolizumab) did not alter PD-L1 surface levels relative to untreated cells. Live cell confocal microscopy imaging of H2444 cells showed that upon treatment with fluorescently labeled TS1521, significant PD-L1 clustering was observed within 3 h, whereas no clustering was observed following treatment with fluorescently labeled atezolizumab (Figure 4D). Visualization of PD-L1 clustering was found to correspond with the

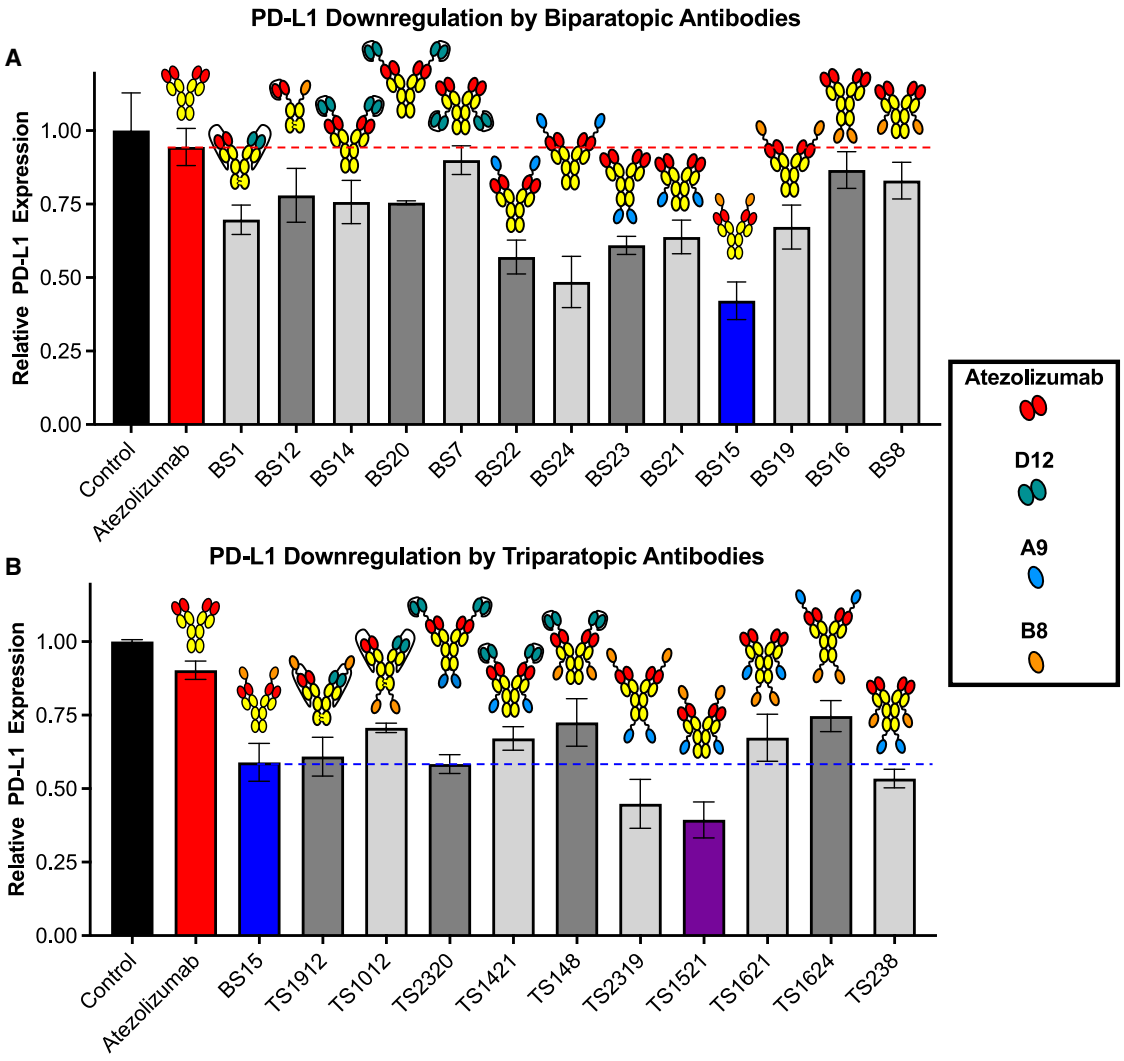

Figure 3. Topology and epitope dependence of antibody-mediated PD-L1 downregulation

(A and B) MDA-MB-231 human breast cancer cells were treated with the specified (A) biparatopic or (B) triparatopic antibody for 12 h, then surface PD-L1 was quantified by flow cytometry. All values were normalized to an untreated control (black). Error bars represent the standard deviation from three replicates. Statistical significance was determined by one-way ANOVA and is presented in Table S4.

See also Figure S4 and Table S4.

steady state kinetic downregulation profile, and internalization occurred (based on flow cytometry analysis) before detectable clustering was observed by microscopy (Figures 4C and 4D). Super resolution (SR) microscopy studies on H2444 cells revealed clustering of labeled TS1521 on the cell membrane at single-molecule resolution (Figures 4E, 4F, and S5). Compared to the more disperse surface distribution of labeled atezolizumab, labeled TS1521 was significantly more clustered, with a median of more than 60% of TS1521 molecules occurring in clusters of 10 or more, compared to less than 40% for atezolizumab (Figure 4G).

As shown in Figure 1A, surface levels of PD-L1 are dictated by the balance between synthesis, internalization, recycling, and degradation of the protein. To determine whether PD-L1 recycling was impacted by multiparatopic antibody treatment, H2444 cells were incubated with TS1521 in the absence or presence of the recycling inhibitor monensin. We observed no change in TS1521-mediated PD-L1 downregulation with or without monensin, suggesting that no recycling was occurring in the presence of the multiparatopic antibody (Figure 5A). Interestingly, there was no difference in PD-L1 surface levels in untreated cells incubated with or without monensin, indicating that recycling was not contributing significantly to the molecular dynamics of this system. We further confirmed that recycling was not impacted by multiparatopic antibody treatment using a pulse-chase quenching assay. In brief, H2444 cells were pulsed with Alexa Fluor 488-labeled antibody (either atezolizumab or TS1521) at 37°C for 2 h to allow for internalization, and then briefly incubated with an anti-Alexa Fluor 488 antibody at 4°C to quench surface staining of PD-L1 while also preventing further internalization. Cells were subsequently returned to 37°C for a chase period in the continued presence of the

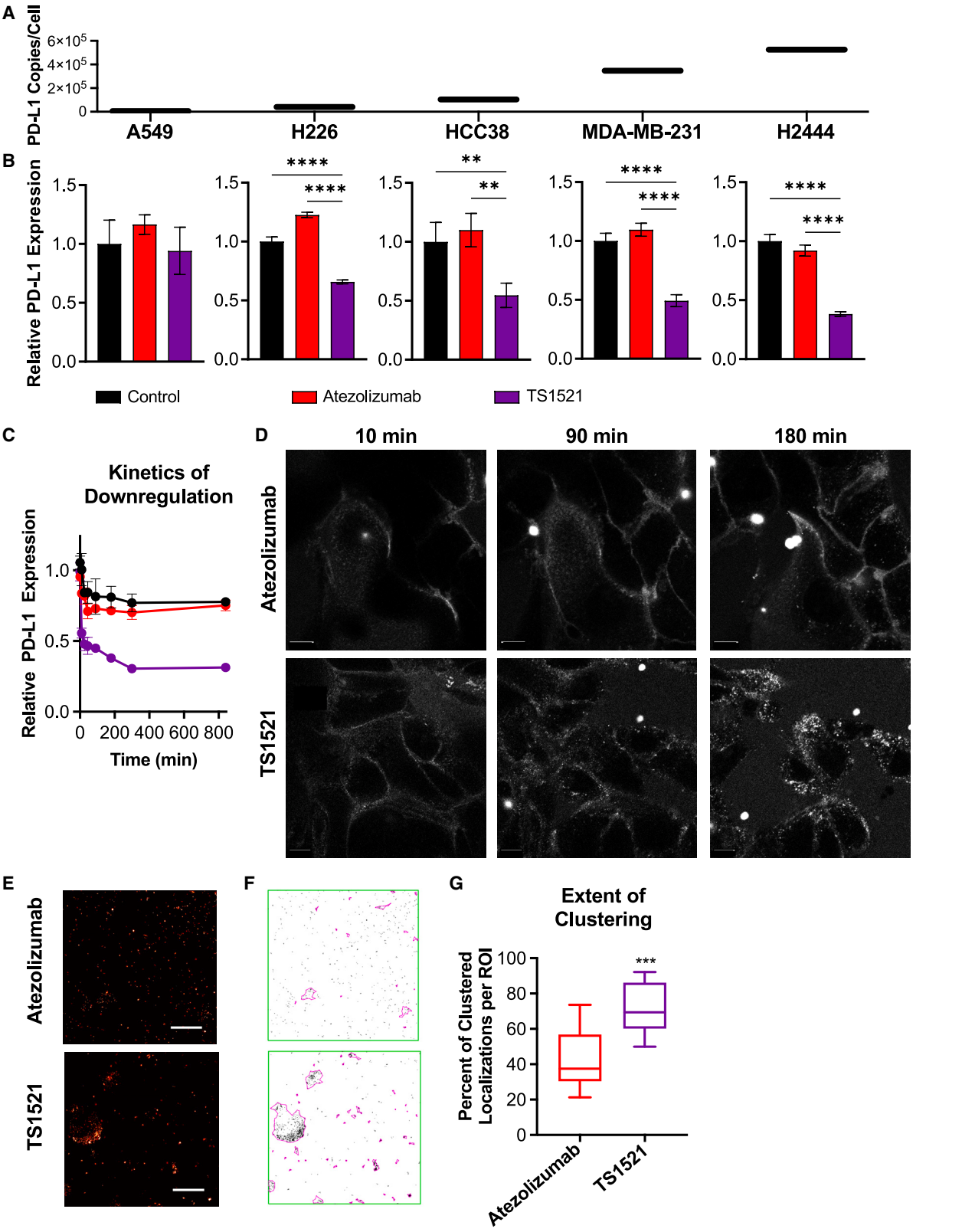

(legend on next page)

quenching antibody, so that a subsequent drop in fluorescent signal would be observed if recycling was occurring. The pulse-chase assay showed that minimal recycling of PD-L1 occurred in cells treated with either atezolizumab or TS1521 (Figure 5B), consistent with the findings of monensin studies. Minimal recycling of PD-L1 was also observed following treatment with BS1. Notably, a less effective multiparatopic downregulating antibody (BS15) was found to enable PD-L1 recycling, perhaps contributing to its inferior efficacy in reducing surface protein levels (Figure S4E). Divergence in PD-L1 recycling in response to treatment with TS1521 versus BS15 further highlights the relevance of topology and epitope engagement in determining how an antibody will influence molecular trafficking.

To delineate the ultimate fate of internalized PD-L1, we separately conjugated the monoclonal antibody atezolizumab and the multiparatopic antibody TS1521 to a pH-sensitive fluorescent dye, which increases in intensity at lower pH ranges characteristic of endosomal and lysosomal compartments. Fluorescence intensity was dramatically higher in H2444 cells treated with TS1521 compared to those treated with atezolizumab over the course of 36 h, indicative of higher endosomal and lysosomal accumulation of PD-L1 in the context of the multiparatopic antibody (Figure 5C). Significant divergence between lysosomal accumulation of the monoclonal versus the multiparatopic antibody was observed within 12 h of treatment. Other multiparatopic antibodies (BS1 and BS15) also induced increased lysosomal trafficking relative to atezolizumab (Figure S4F), and the extent of lysosomal accumulation corresponded to downregulation efficiency of the respective antibodies (Figure 3). Confocal microscopy was performed to visualize subcellular localization of fluorescently labeled anti-PD-L1 monoclonal or multiparatopic antibodies after a 14-h-incubation with H2444 cells (Figures 5D and S4G–S4H). Atezolizumab treatment resulted in a diffuse cell surface distribution of PD-L1, displaying minimal association of the antibody with endosomal marker early endosome antigen 1 (EEA1) or the lysosomal marker lysosome-associated membrane glycoprotein 1 (LAMP1), which is also present—albeit at lower levels—on late endosomes. In contrast, TS1521 treatment resulted in extensive PD-L1 clustering across focal plans, with substantial evidence of both endosomal and lysosomal colocalization of the antibody. Image quantification reinforced the observed enhancement of endosomal and lysosomal trafficking of PD-L1, and the fraction of lysosomes associated with PD-L1 was nearly 3-fold higher after treatment with TS1521 compared to treatment with atezolizumab (Figure 5E). Taken together, trafficking studies established that PD-L1-targeted multiparatopic antibodies orchestrate downregulation by enhancing PD-L1 endocytosis and lysosomal sorting, with recycling playing a minimal role in regulating surface protein levels.

PD-L1-targeted multiparatopic antibody treatment leads to enhanced immune cell activity

Based on our observation that engineered multiparatopic antibodies downregulate PD-L1, we sought to determine whether this feature could be exploited to inhibit the immunosuppressive activities of the PD-1/PD-L1 pathway. As an initial test of the immunostimulatory capacity and consequent immunotherapeutic potential for multiparatopic antibodies, we compared the performance of the monoclonal antibody atezolizumab and the multiparatopic antibody TS1521 in a commercially acquired T cell receptor (TCR) activation reporter assay (Promega). In brief, the assay consists of 2 cell lines: Chinese hamster ovary (CHO)-K1 cells that stably express PD-L1 and a cell surface protein which elicits antigen-specific TCR activation (serving as APCs); and human Jurkat T cells with cognate TCRs that stably express PD-1 and an NFAT-inducible luciferase reporter (serving as effector cells). The APCs were first incubated with either atezolizumab or TS1521 for 2 h to allow for PD-L1 downregulation. In some samples, the antibody was then removed, followed by addition of PD-1-expressing effector cells, whereas in other samples the antibody was still present after the addition of effector cells. NFAT-induced luminescence was used as a readout for TCR activation enabled by antibody-mediated blockade of PD-1/PD-L1 signaling. In samples wherein the antibody was continuously present, TS1521 was slightly less potent in eliciting TCR activation compared to atezolizumab (EC_{50} = 0.51 vs. 0.30 nM) (Figure 6A; Table S2), which parallels the PD-L1 binding affinity data (Figures S6A and S6B; Table S1). However, when the antibody was removed prior to addition of the effector cells, TS1521 led to more potent activation of TCR compared to atezolizumab (0.95 vs. 1.6 nM). The more dramatic reduction in TCR activation

Figure 4. Antibody-induced clustering and internalization of PD-L1

(A) Quantification of PD-L1 receptor expression on 5 human cancer cell lines via flow cytometry.

(B) The indicated cells were treated with atezolizumab (red) or the multiparatopic antibody TS1521 (purple) for 12 h, and then surface PD-L1 was quantified by flow cytometry. Data were normalized relative to an untreated control (black). Error bars represent SD (n = 3), and significance was determined by one-way ANOVA.

(C) H2444 cells were exposed to atezolizumab (red), TS1521 (purple) or were left untreated (black) for varying time periods. Surface receptor levels were quantified by flow cytometry. Error bars represent SD (n = 3).

(D) Confocal imaging of PD-L1 on live H2444 human lung cancer cells treated with Alexa Fluor 488-conjugated atezolizumab or TS1521 at different time points. The scale bars measure 14 μm.

(E) Representative regions of interest (ROIs) sampled from super resolution (SR) imaging data of H2444 cells treated with Alexa Fluor 647-conjugated atezolizumab or TS1521 for 12 h. The scale bars measure 1,000 nm. The dots on these images are Gaussian representations of the point spread function for each localization detected.

(F) Cluster boundaries (in magenta) found by DBSCAN superposed on top of the SR localization locations (black points) from the SR images shown in (E). The green boxes define the ROI boundaries. The points that fall outside the magenta boundaries are counted as not clustered. DBSCAN was run with parameters epsilon = 100 nm, minimum number of localizations to form a cluster = 10.

(G) Boxplot depicting the percent of clustered localizations per ROI for H2444 cells treated with atezolizumab and TS1521, determined as shown in (F). In this plot, the middle bars indicate the median, the edges of the boxes extend from the 25th to the 75th percentiles of the data, and the whiskers reach to the most extreme data. Significance was determined by two-sample Kolmogorov-Smirnov goodness-of-fit hypothesis test. Results from all statistical tests are shown in Table S4.

See also Figures S4 and S5, Table S4, Videos S1, and S2.

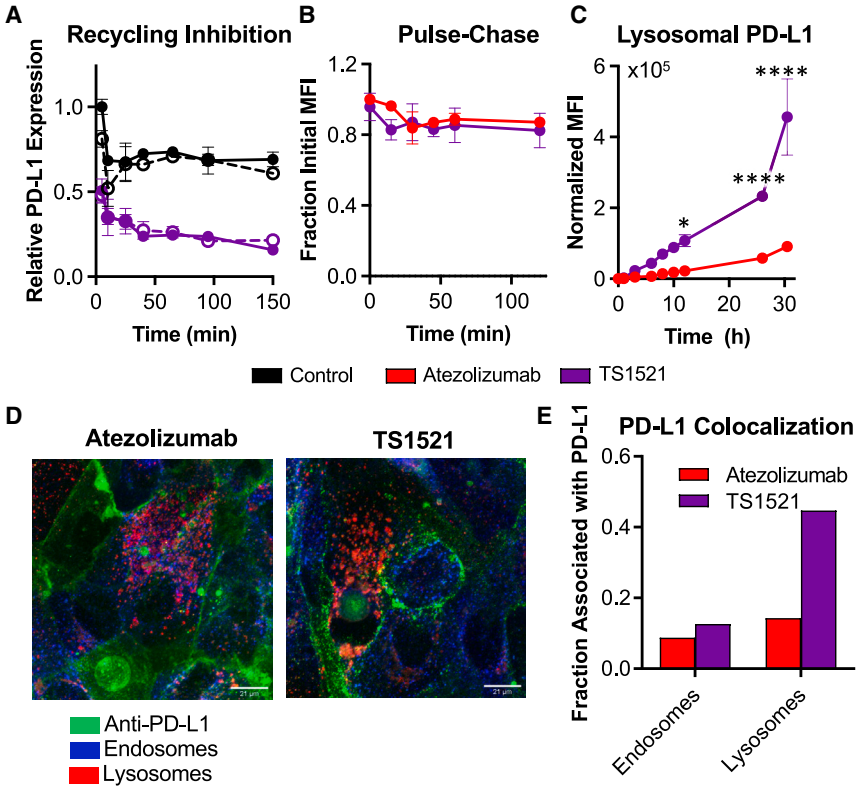

Figure 5. Antibody-mediated effects on PD-L1 trafficking and subcellular localization

(A) Surface PD-L1 expression time course in H2444 cells treated with TS1521 (purple) or untreated control (black) in either the presence (closed circles) or absence (open circles) of the recycling inhibitor monensin. Error bars represent SD (n = 3).

(B) H2444 cells were pulsed with Alexa Fluor 488-conjugated atezolizumab (red) or TS1521 (purple) for 2 h at 37°C, followed by quenching of surface signal at 4°C. Cells were then chased at 37°C in the continued presence of quenching antibody for the indicated time period, such that further decreases in signal would reflect recycling of internalized PD-L1. Data are plotted normalized to surface PD-L1 signaling following the initial quenching reaction. Error bars represent SD (n = 3).

(C) H2444 cells were treated with either atezolizumab (red) or TS1521 (purple) conjugated to a pH-sensitive fluorescent dye for the indicated amount of time. Error bars represent SD (n = 3). Significance was determined by two-way ANOVA.

(D) Confocal microscopy imaging of H2444 cells treated with Alexa Fluor 488-conjugated atezolizumab or TS1521 (green) for 13 h, then stained for endosomes (blue, EEA1) and lysosomes (red, LAMP-1) to assess colocalization. The scale bars measure 21 μm.

(E) Fraction of endosomes and lysosomes from images presented in (D) that are associated with atezolizumab (red) or TS1521 (purple). Results from all statistical tests are shown in Table S4.

See also Table S4.

potency for atezolizumab versus TS1521 in the continued presence versus removal of antibody (5.3-fold versus 1.9-fold reduction) suggests that the downregulation effect of the multiparatopic antibody bolsters the durability of PD-1/PD-L1 blockade.

We next sought to determine whether the improvement in immune effector cell activation for multiparatopic versus monoclonal antibodies would extend to a primary cell system. To this end, we treated human peripheral blood mononuclear cells (PBMCs) isolated from hepatitis C virus (HCV)-infected donors from time points at which high T cell PD-1 expression was measured.[53] This cohort was chosen due to expression of high levels of PD-1 on T cells, and all specimens were tested that contained sufficient cell numbers for analysis. PBMCs were treated with either atezolizumab or TS1521 for 1 h to allow for PD-L1 downregulation. The antibodies were then either retained or washed off. PBMCs were then stimulated with HCV-derived peptides and ELISpot assays were performed to identify the number of IFN-γ-producing cells as a measurement of immune effector cell activation (Figures 6B and S6C). In donor 175, an increase in the number of IFN-γ-secreting cells was observed following continuous treatment with either atezolizumab or TS1521. However, in samples where the antibody was removed prior to stimulation, atezolizumab-treated cells returned to baseline levels of stimulation. In contrast, TS1521-treated samples maintained elevated levels of effector cell activity even when the antibody was removed. As in the TCR activation reporter assay, the reduced sensitivity to antibody removal for TS1521 versus atezolizumab indicates that our engineered multiparatopic antibody enhances immune checkpoint blockade through downregulation of PD-L1. Studies on a second donor (donor 29) corroborated the observed increase in the number of IFN-γ-secreting effector cells upon treatment with either atezolizumab or TS1521, and the increase was more pronounced for the multiparatopic versus the monoclonal antibody. Collectively, immune cell signaling assays on both immortalized cell lines and primary human cells illustrate the potential for our strategy to enhance immune checkpoint blockade by recruiting a trafficking-focused mechanism in addition to competitive inhibition.

Multiparatopic antibodies exhibit robust tumor localization and durably attenuate PD-L1 availability in mouse cancer models

Building on the promising immunostimulatory effects of our PD-L1-targeted multiparatopic antibody in cellular studies, we sought to examine the biodistribution and pharmacokinetic properties of TS1521 in a mouse tumor xenograft model. We compared tumor trafficking of systemically (i.v.) injected atezolizumab and TS1521 in non-obese diabetic scid gamma (NSG) mice bearing MD-MBA-231 tumors were via near infrared imaging (Figures 7A and 7B). No major differences in the specificity or persistence of tumor localization were observed over time between the antibodies, affirming that our engineered multiparatopic antibody recapitulates the biodistribution and pharmacokinetic properties of the clinical anti-PD-L1 monoclonal antibody. Finally, we tested whether our multiparatopic antibody could reduce the bioavailability of PD-L1 in a mouse tumor model. To do this, we leveraged a recently developed approach that detects radiolabeled peptides which bind PD-L1 at the PD-1/PD-L1

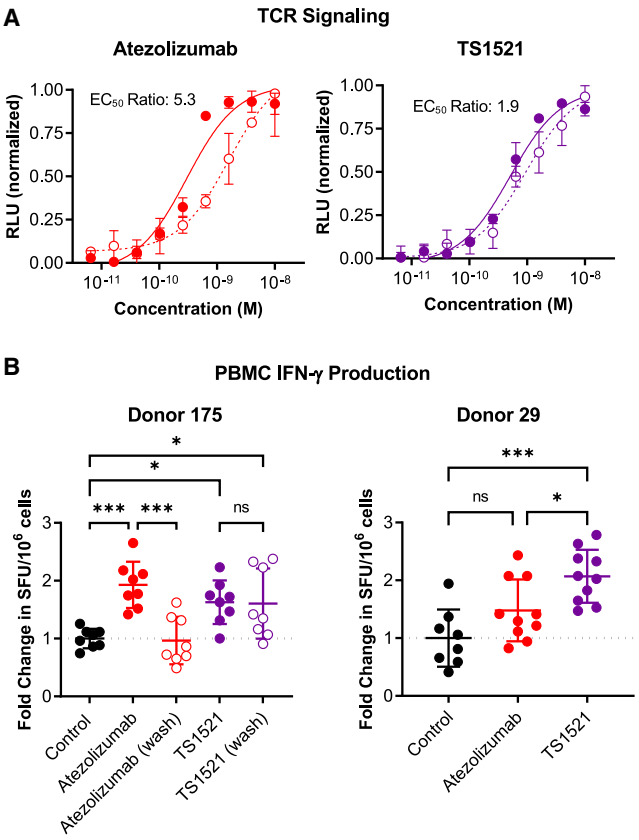

Figure 6. Enhancement of immune cell activation following antibody-mediated downregulation of PD-L1

(A) Activation readouts from a commercial TCR signaling reporter assay. Atezolizumab (red, left) or TS1521 (purple, right) was added to PD-L1-expressing antigen-presenting cells (APCs) for 2 h to allow for downregulation to occur. Subsequently, the antibodies were maintained in some samples (solid lines), while in others the antibody was washed away (dotted lines). The APCs were then incubated with effector (Jurkat) cells, and NFAT-induced luminescence was used a readout for TCR signaling, reflecting the extent of PD-1/PD-L1 blockade. Error bars represent SD (n = 3).

(B) Activation readouts from a primary human T cell functional assay. PBMCs from two human donors with T cells specific for HCV peptides were first treated with either atezolizumab (red) or TS1521 (purple), then stimulated with peptide in either the continued presence of the antibody (closed circles), or with the antibody washed off (wash, open circles). Activation was quantified by ELISpot analysis of interferon-γ secretion. The signal reported is normalized to the untreated control, and combines data from two identical experiments. Error bars represent SD. Significance was determined by one-way ANOVA. Detailed statistical results are shown in Table S4.

See also Figure S6, Tables S3 and S4.

binding interface in order to quantify the amount of cell surface PD-L1 that is *not* bound to a PD-L1-competitive antibody and therefore ostensibly available for signaling.[54] Mice were implanted orthotopically with MDA-MB-231 tumor cells and divided into groups of equally sized tumors after tumors were palpable (Figure S7A). At time points of 1- and 4-days following a single antibody injection, availability of PD-L1 was found to be significantly decreased in animals treated with TS1521 compared to untreated control animals (Figure 7C). Although PD-L1 availability increased on day 4 compared to day 1, significant reduction was maintained compared to untreated control mice, confirming the durable effects of our engineered multiparatopic antibody in suppressing the PD-1/PD-L1 pathway. We observed that despite its lower affinity for PD-L1 (Figure S6A), TS1521 performed equivalently to atezolizumab in blocking PD-L1 availability *in vivo*, as shown in Figure S7B, indicating that superior downregulation induction may contribute to the inhibitory activity of TS1521 in this model. These results were confirmed by positron emission tomography (PET) imaging (Figure S7C). Adjustment of dosing amount and frequency will be required to optimize the *in vivo* inhibitory activity of TS1521 in future studies.

DISCUSSION

The concept of promoting cell surface protein clustering using multiparatopic antibodies has been reported previously[31–38] and presents a promising mechanism to hijack innate trafficking pathways for targeted degradation of transmembrane proteins. Moreover, this mechanism is complementary to and synergistic with competitive inhibition of ligand/receptor interactions. However, most studies have focused on receptor tyrosine kinases, with limited exploration of systems beyond this family of proteins. In this study, we hypothesized that the multiparatopic antibody approach could be applied to a new class of proteins, specifically immune checkpoint proteins, to relieve cancer-mediated suppression of T cell activity. Our results established that multiparatopic antibody-mediated downregulation can be achieved in the PD-L1 system, and that this effect leads to enhanced immune cell stimulation and sustained suppression of PD-L1 in mouse tumor models.

Consistent with previous results in designing multiparatopic antibodies that target other surface proteins, induced downregulation depends on a variety of molecular factors, including the specific binding epitopes that are targeted and antibody fusion topology[31,32] (Figure 3). With respect to epitope, several prominent themes emerged in our study. First, we observed that combining non-competitive epitopes (e.g., atezolizumab and A9) led to superior PD-L1 downregulation compared to use of overlapping epitopes (e.g., atezolizumab and D12). This finding was consistent with previous observations for receptor tyrosine kinases,[31,33] and it implies that target protein cross-linking is essential to the downregulation mechanism. Second, we established that certain combinations of binding domains (e.g., atezolizumab and A9) more actively downregulated PD-L1 compared to others (e.g., atezolizumab and B8). Finally, we found that constructs comprising 3 non-competitive binding domains led to more efficient target downregulation compared to constructs comprising 2 non-competitive binding domains, in agreement with observations in the EGFR system.[31] Regarding antibody topology, we demonstrated that subtle differences in orientation can have profound effects on downregulation induction. Slight modifications such as relocation of fusion from the N-terminus of the HC to the N-terminus of the LC of an antibody, a distance far shorter than the flexible linker connecting the domains, could lead to significantly different downregulation outcomes (e.g., BS15 versus BS19, $p = 0.0088$), although these differences were only observed for certain epitope combinations (e.g., differences were not observed for BS22 versus BS24, $p = 0.9685$). We

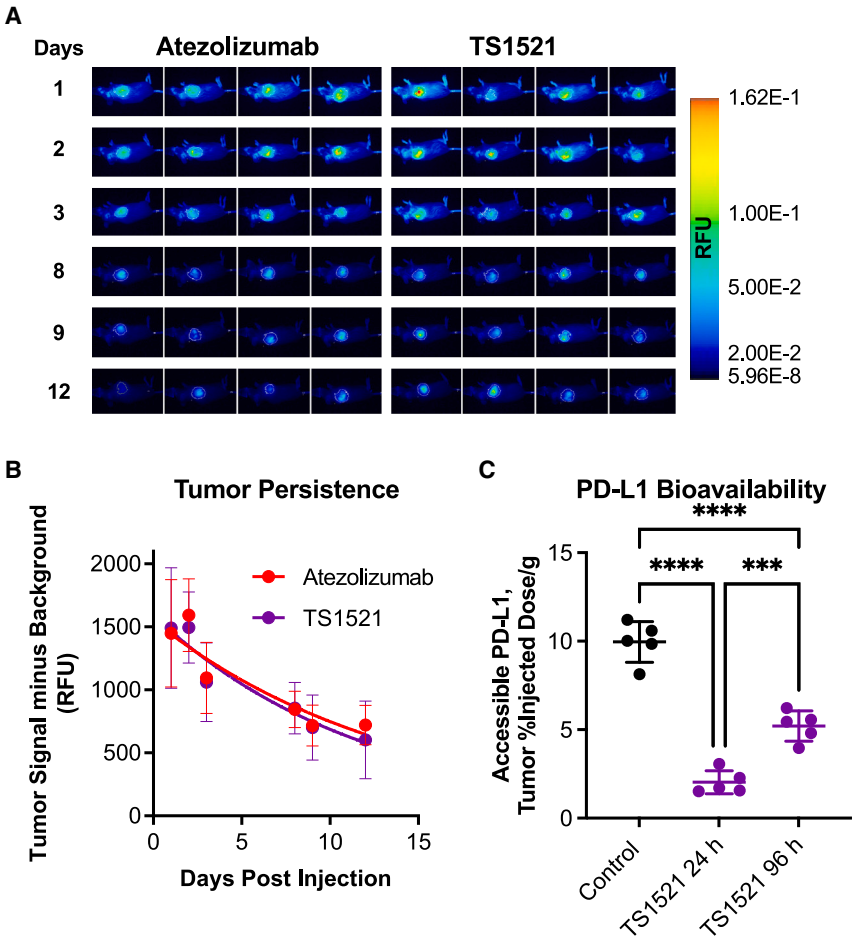

Figure 7. *In vivo* pharmacodynamics of PD-L1-targeted multiparatopic antibody

(A) Antibody localization and persistence in MDA-MB-231 tumors in NSG mice after i.v. (tail vein) injection of 10 mg/kg near-infrared (IR) dye-labeled atezolizumab or TS1521, detected by LI-COR imaging.

(B) Quantification of antibody persistence in the tumor over time from (A). Error bars represent SD (n = 4).

(C) Bioavailability of tumor PD-L1. NSG mice bearing MDA-MB-231 tumors were injected i.v. with 1 mg/kg TS1521 for 24 or 96 h. Surface PD-L1 that was not bound to a PD-1 competitive antibody (i.e., bioavailable PD-L1) was quantified using a radiolabeled peptide.[54] Significance was determined by one-way ANOVA, further statistical results are included in Table S4.

See also Figure S7 and Table S4.

further found that multivalent representation of each binding domain was not required for downregulation, as constructs incorporating monovalent binding for one of the anti-PD-L1 domains successfully mediated downregulation (e.g., BS1 and BS12). For triparatopic antibodies, binding domain orientation and not just the particular combination of domains used was found to impact extent of downregulation, as distinct effects were observed for different permutations of the atezolizumab, A9, and B8 domains (e.g., TS1521 versus TS1621 ($p < 0.0001$)). Thus, although there is a clear dependency of PD-L1 downregulation on antibody topology, the effects cannot always be predicted by inspection of structural layout alone. It is also worth noting that the PD-L1 affinities of the newly discovered VNARs are significantly weaker than that of the approved drug atezolizumab, and it would be interesting to engineer affinity variants of these binding domains and compare downregulation efficiency of multiparatopic combinations thereof in future work.

In addition to dependence on antibody design, extent of downregulation is also impacted by other factors, such as target protein expression levels. We found that the extent of downregulation increased with target protein surface density (Figures 4A, 4B, S4A, and S4B), consistent with the requirement for a threshold number of cell surface expression in order to achieve antibody-mediated cross-linking and consequent downregulation. Interestingly, this is the opposite of what was observed for the EGFR system, wherein the extent of downregulation decreased with increasing target protein surface density.[31,55] However, it should be noted that the range of surface densities sampled differed between these 2 studies: the current study with PD-L1 examined cell lines with surface densities ranging from 5,800 to 530,000 proteins/cell whereas previous work with EGFR examined cell lines with surface densities ranging from 100,000 proteins/cell to 2,800,000 proteins/cell. Taken together, these 2 multiparatopic antibody studies consistently suggest an optimum level of target protein expression for maximal downregulation in the range of 100,000–600,000 proteins/cell. This range is on the higher end of the PD-L1 expression levels on cancer cell lines studied herein, and PD-L1 expression levels in the tumor microenvironment are likely to fall in this range, as cells in the tumor context have been shown to upregulate PD-L1 compared to cultured cell lines due to the presence of IFN-γ.[9] For cells that express >600,000 receptors per cell, as was observed for certain EGFR-expressing cell lines,[31,55] it is possible that the downregulation machinery may become saturated or that antibody-mediated clustering may become less efficient due to crowding effects. Future studies will probe the downregulation activity of our engineered multiparatopic antibodies in additional cancer types. The increased internalization with increasing target protein surface density in the case of PD-L1 could be leveraged for improved cell selectivity of multiparatopic antibodies, as seen in the case of HER2.[56] Other possible factors that could modulate the downregulation efficiency of TS1521 are the proteins CMTM4 and CMTM6, which are ubiquitously expressed and colocalized in the membrane to stabilize PD-L1 and protect it from degradation.[57] This phenomenon will be interesting to explore in future studies. We further note that the effects of target protein surface density are also dependent on antibody topology, as TS1521 and

TS2319 induce similar levels of downregulation on cell lines with high levels of PD-L1 but only TS1521 induces significant downregulation on cell lines that express lower PD-L1 levels, such as H226 (Figures 4B and S4A). This finding suggests that altering the topology could be leveraged to tune downregulation effects toward cell populations with differential target protein expression levels. Collectively, our findings argue for the importance of considering antibody structure, orientation, valency, and target expression profile in the design of therapeutic multiparatopic antibodies.

Previous work has generally shown that multiparatopic antibody-induced downregulation may increase rates of internalization, decrease rates of recycling, or both.[31–38] Here, we report that at least one of the antibody constructs we created (BS15) actually increased the rate of recycling compared to both treatment with a monoclonal antibody and untreated PD-L1 (Figure S4E). Incidentally, BS15 was also the most effective biparatopic antibody, implying that the antibody compensated for its proclivity toward PD-L1 recycling rather than degradation by dramatically increasing internalization rates. Further exploration of preferential partitioning toward recycling versus degradation pathways for various multiparatopic constructs could inform our understanding of and ability to manipulate PD-L1 trafficking in order to regulate immune behavior.

To probe the translational potential for multiparatopic antibody strategies targeting PD-L1, we assessed the immunomodulatory activities of our lead construct in both cellular and animal models. Studies in both immortalized cell lines and primary human immune cells illustrated the advantage for multiparatopic relative to monoclonal anti-PD-L1 antibodies in terms of potency and durability of PD-1/PD-L1 pathway suppression resulting from the combined mechanisms of competitive inhibition and downregulation (Figure 6). Encouragingly, pharmacokinetics of our lead construct in a mouse model of breast cancer revealed that TS1521 exhibits similar tumor-targeting and tumor persistence properties compared to the clinical monoclonal antibody atezolizumab (Figures 7A and 7B). Furthermore, using a recently reported imaging approach,[54] we found that TS1521 led to significant and durable suppression of PD-L1 bioavailability (Figure 7C). While the recently reported antitumor efficacy of a small molecule that internalizes PD-L1 supports the relevance of trafficking modulation in ICI therapies,[39] future *in vivo* studies will using immunocompetent and translationally relevant models of cancer be required to establish the immunotherapeutic activities of the multiparatopic antibodies we designed.

One potential concern for our multi-faceted approach is that it could lead to an increase in immunotherapy-related adverse events (irAEs). A recent report by Zhang and colleagues demonstrates increased irAEs related to lysosomal trafficking of CTLA-4 following ICI antibody treatment.[40] However, unlike CTLA-4, which is known to rapidly cycle between the surface and intracellular compartments, our data suggest that PD-L1 has minimal rates of recycling in either untreated or antibody-treated cells (Figures 5A and 5B). Therefore, we anticipate, suggesting that increased lysosomal degradation would not disproportionately impact the balance of pre-existing internal PD-L1 stores that are needed to coordinate peripheral tolerance.

In addition to previously discussed mechanisms, the rapid formation of antibody/PD-L1 clusters on the tumor cell surface could potentially serve to enhance antibody-dependent cellular cytotoxicity (ADCC). While the multiparatopic antibodies we designed here have impaired Fc effector function, the clinical anti-PD-L1 antibody avelumab has fully intact Fc effector activities and has been shown to mediate tumor cell lysis by NK cells in a PD-L1 density-dependent manner.[58,59] Clustering of multiparatopic antibodies on the surface of tumor cells could increase Fc-mediated immune cell recruitment and ADCC-induced tumor cell lysis, presenting a third concurrent antitumor mechanism for our engineered constructs.

Recently, there has been a surge of interest in harnessing endogenous machinery to promote internalization of cell surface proteins for various purposes, such as targeted elimination or payload delivery. Many promising strategies have emerged in the area of targeted protein degradation, including platforms such as antibody-based proteolysis-targeting chimeras (AbTACs), which cross-link a target transmembrane protein with a ubiquitin ligase to induce proteosomal degradation,[60] and lysosome-targeting chimeras (LYTACs),[61] which colocalize a target protein with a lysosome-shuttling receptor to coordinate lysosomal degradation. Our strategy presents a streamlined alternative to these targeted protein degradation approaches in that it does not require the expression or engagement of a second target protein in the cell membrane, which could improve specificity and efficiency, while also allowing for broader application. There has also been tremendous progress in the field of antibody-drug conjugates (ADCs), which link a cytotoxic drug payload to a monoclonal antibody to achieve targeted destruction of diseased cells following binding and internalization of the ADC.[62] Future extensions of our technology could combine our multiparatopic approach with ADC strategies to promote internalization of PD-L1 for enhanced delivery of the cytotoxic payload. Indeed, a HER2-targeted biparatopic ADC was found to induce regression of refractory tumors in preclinical models of breast cancer.[56] Furthermore, since our multiparatopic antibodies are composed of newly discovered anti-PD-L1 domains with lower target affinity compared to the approved antibody therapeutic atezolizumab (Figure 2A), these molecules could potentially exhibit enhanced tumor penetration, as faster rates of dissociation (Table S2) have been shown to result in a more homogeneous distribution in solid tumors.[63,64] Overall, we have established a new class of ICI antibodies that acts through a distinct trafficking-focused mechanism and identified an optimized format for blocking T cell suppressive pathways, which could inform the development of more effective immunotherapies.

Limitations of the study

This study provides key proof of concept that multiparatopic antibodies that target multiple epitopes on PD-L1 induce robust internalization and degradation of the target protein, leading to enhanced immune cell activation compared to the FDA-approved monoclonal antibody atezolizumab. Preliminary *in vivo* studies showed that multiparatopic antibody-mediated downregulation leads to sustained suppression of PD-L1 bioavailability in mouse tumor xenograft models. However, due to the lack of reactivity between our newly discovered anti-human PD-L1 VNARs and mouse PD-L1, these molecules will need to be investigated further using humanized mouse models. Development

and implementation of such immunocompetent and translationally meaningful models will be required to demonstrate the therapeutic benefit for our engineered multiparatopic antibody relative to current clinical ICI antibodies. In addition, *in vivo* mechanistic studies will be required to demonstrate the immunostimulatory effects of our intervention, again compared to currently approved therapies. A further consideration for our molecule is the need for rigorous biophysical and biochemical characterization to ensure developability and enable scalable production of the antibody. Overall, this work represents a first step toward harnessing endogenous protein trafficking machinery to establish new mechanisms for immunotherapy.

SIGNIFICANCE

Immune checkpoint inhibitor antibodies have revolutionized the cancer treatment landscape and have shown clinical success across a range of solid tumor and hematological malignancies. However, tumor regression is uneven across patients and overall response rates remain low, motivating the need for new mechanistic insights regarding immunosuppressive pathways. We report the development of multiparatopic antibodies against the immune checkpoint protein programmed death-ligand 1 (PD-L1) and show that these antibodies: (1) induce clustering, internalization, and degradation of PD-L1 in a topology- and epitope-dependent manner; (2) effect more potent immune cell activation than a clinical monoclonal antibody; and (3) suppress PD-L1 availability in mouse tumor models. Our findings offer insights into the impact of trafficking mechanisms on the PD-L1/PD-1 axis and present a roadmap for the design of immunomodulatory therapeutics.

STAR★METHODS

Detailed methods are provided in the online version of this paper and include the following:

- KEY RESOURCES TABLE
- RESOURCE AVAILABILITY
  - Lead contact
  - Materials availability
  - Data and code availability
- EXPERIMENTAL MODEL AND STUDY PARTICIPANT DETAILS
  - Cell lines
  - Human PBMCs
  - Mice
- METHOD DETAILS
  - Protein expression and purification
  - Protein stability tests
  - Yeast surface binding studies
  - Shark immunizations
  - IgNAR antigen-binding ELISAs
  - cDNA synthesis
  - VNAR library cloning
  - Yeast library selections
  - Bio-layer interferometry
  - Quantification of target expression
  - Receptor downregulation assays
  - Pulse-chase assays
  - Lysosomal accumulation assays
  - Confocal microscopy
  - Super Resolution (SR) imaging
  - Super Resolution (SR) image analysis
  - Cluster analysis
  - Cell surface binding studies
  - PD-1/PD-L1 blockade TCR activation reporter cell assay
  - ELISpot T-Cell Activation Assay
  - Mouse pharmacokinetic and biodistribution studies
- QUANTIFICATION AND STATISTICAL ANALYSIS

SUPPLEMENTAL INFORMATION

Supplemental information can be found online at https://doi.org/10.1016/j.chembiol.2024.02.014.

ACKNOWLEDGMENTS

The authors acknowledge a V Foundation V Scholar Award (J.B.S.), the Emerson Collective Cancer Research Fund (J.B.S), a Damon Runyon-Rachleff Innovation Award (J.B.S.), NIH (R01CA236616 and R01CA269235 to S.N.; R21CA249381 to J.B.S.), a Johns Hopkins University Catalyst Award, and a National Science Foundation CAREER Award (2143160 to J.B.S.) for support. Microscopy was supported by the Wilmer Core Grant, Microscopy module, EY001765.

AUTHOR CONTRIBUTIONS

S.D.L., B.M., J.T., R.K., K.J.K., A.Z., and H.M.D. discovered and characterized antibody binding fragments; S.D.L. and J.B.S. designed multiparatopic antibodies; S.D.L. conducted downregulation and trafficking assays; S.D.L. conducted confocal microscopy; G.S. conducted ELISpot assays and A.L.C. oversaw and interpreted these studies; A.M. conducted *in vivo* biodistribution assays and S.N. oversaw and interpreted these studies; S.J.L. performed TCR activation assays; D.J.S., M.J.W., and K.A.L. conducted STORM imaging; S.D.L., A.M., G.S., A.L.C., S.N., and J.B.S. designed experiments and interpreted data; S.D.L. and J.B.S. wrote the manuscript. All authors reviewed and provided feedback on manuscript drafts.

DECLARATION OF INTERESTS

The authors have filed intellectual property covering the technologies described herein (patent number PCT/US2023/072013).

Received: August 12, 2023
Revised: December 28, 2023
Accepted: February 28, 2024
Published: March 27, 2024; Corrected online: April 22, 2024

REFERENCES

1. Dong, H., Zhu, G., Tamada, K., and Chen, L. (1999). B7-H1, a third member of the B7 family, co-stimulates T-cell proliferation and interleukin-10 secretion. Nat. Med. *5*, 1365–1369. https://doi.org/10.1038/70932.
2. Freeman, G.J., Long, A.J., Iwai, Y., Bourque, K., Chernova, T., Nishimura, H., Fitz, L.J., Malenkovich, N., Okazaki, T., Byrne, M.C., et al. (2000). Engagement of the Pd-1 Immunoinhibitory Receptor by a Novel B7 Family Member Leads to Negative Regulation of Lymphocyte Activation. J. Exp. Med. *192*, 1027–1034.
3. Keir, M.E., Liang, S.C., Guleria, I., Latchman, Y.E., Qipo, A., Albacker, L.A., Koulmanda, M., Freeman, G.J., Sayegh, M.H., and Sharpe, A.H. (2006). Tissue expression of PD-L1 mediates peripheral T cell tolerance. J. Exp. Med. *203*, 883–895. https://doi.org/10.1084/jem.20051776.

4. Nishimura, H., Nose, M., Hiai, H., Minato, N., and Honjo, T. (1999). Development of Lupus-like Autoimmune Diseases by Disruption of the PD-1 Gene Encoding an ITIM Motif-Carrying Immunoreceptor. Immunity *11*, 141–151. https://doi.org/10.1016/S1074-7613(00)80089-8.

5. Dong, H., Strome, S.E., Salomao, D.R., Tamura, H., Hirano, F., Flies, D.B., Roche, P.C., Lu, J., Zhu, G., Tamada, K., et al. (2002). Tumor-associated B7-H1 promotes T-cell apoptosis: A potential mechanism of immune evasion. Nat. Med. *8*, 793–800. https://doi.org/10.1038/nm730.

6. Tamura, H., Ishibashi, M., Yamashita, T., Tanosaki, S., Okuyama, N., Kondo, A., Hyodo, H., Shinya, E., Takahashi, H., Dong, H., et al. (2013). Marrow stromal cells induce B7-H1 expression on myeloma cells, generating aggressive characteristics in multiple myeloma. Leukemia *27*, 464–472. https://doi.org/10.1038/leu.2012.213.

7. Kondo, A., Yamashita, T., Tamura, H., Zhao, W., Tsuji, T., Shimizu, M., Shinya, E., Takahashi, H., Tamada, K., Chen, L., et al. (2010). Interferon-γ and tumor necrosis factor-α induce an immunoinhibitory molecule, B7-H1, via nuclear factor-κB activation in blasts in myelodysplastic syndromes. Blood *116*, 1124–1131. https://doi.org/10.1182/blood-2009-12-255125.

8. Yamamoto, R., Nishikori, M., Kitawaki, T., Sakai, T., Hishizawa, M., Tashima, M., Kondo, T., Ohmori, K., Kurata, M., Hayashi, T., and Uchiyama, T. (2008). PD-1–PD-1 ligand interaction contributes to immunosuppressive microenvironment of Hodgkin lymphoma. Blood *111*, 3220–3224. https://doi.org/10.1182/blood-2007-05-085159.

9. Taube, J.M., Anders, R.A., Young, G.D., Xu, H., Sharma, R., McMiller, T.L., Chen, S., Klein, A.P., Pardoll, D.M., Topalian, S.L., and Chen, L. (2012). Colocalization of Inflammatory Response with B7-H1 Expression in Human Melanocytic Lesions Supports an Adaptive Resistance Mechanism of Immune Escape. Sci. Transl. Med. *4*, 127ra37. https://doi.org/10.1126/scitranslmed.3003689.

10. Pardoll, D.M. (2012). The blockade of immune checkpoints in cancer immunotherapy. Nat. Rev. Cancer *12*, 252–264. https://doi.org/10.1038/nrc3239.

11. Topalian, S.L., Drake, C.G., and Pardoll, D.M. (2015). Immune checkpoint blockade: a common denominator approach to cancer therapy. Cancer Cell *27*, 450–461. https://doi.org/10.1016/j.ccell.2015.03.001.

12. Topalian, S.L., Hodi, F.S., Brahmer, J.R., Gettinger, S.N., Smith, D.C., McDermott, D.F., Powderly, J.D., Carvajal, R.D., Sosman, J.A., Atkins, M.B., et al. (2012). Safety, Activity, and Immune Correlates of Anti–PD-1 Antibody in Cancer. N. Engl. J. Med. *366*, 2443–2454. https://doi.org/10.1056/NEJMoa1200690.

13. Brahmer, J.R., Tykodi, S.S., Chow, L.Q.M., Hwu, W.-J., Topalian, S.L., Hwu, P., Drake, C.G., Camacho, L.H., Kauh, J., Odunsi, K., et al. (2012). Safety and Activity of Anti–PD-L1 Antibody in Patients with Advanced Cancer. N. Engl. J. Med. *366*, 2455–2465. https://doi.org/10.1056/NEJMoa1200694.

14. Herbst, R.S., Soria, J.-C., Kowanetz, M., Fine, G.D., Hamid, O., Gordon, M.S., Sosman, J.A., McDermott, D.F., Powderly, J.D., Gettinger, S.N., et al. (2014). Predictive correlates of response to the anti-PD-L1 antibody MPDL3280A in cancer patients. Nature *515*, 563–567. https://doi.org/10.1038/nature14011.

15. Barber, D.L., Wherry, E.J., Masopust, D., Zhu, B., Allison, J.P., Sharpe, A.H., Freeman, G.J., and Ahmed, R. (2006). Restoring function in exhausted CD8 T cells during chronic viral infection. Nature *439*, 682–687. https://doi.org/10.1038/nature04444.

16. Gajewski, T.F., Louahed, J., and Brichard, V.G. (2010). Gene Signature in Melanoma Associated With Clinical Activity: A Potential Clue to Unlock Cancer Immunotherapy. Cancer J. *16*, 399–403. https://doi.org/10.1097/PPO.0b013e3181eacbd8.

17. Kleinovink, J.W., Marijt, K.A., Schoonderwoerd, M.J.A., van Hall, T., Ossendorp, F., and Fransen, M.F. (2017). PD-L1 expression on malignant cells is no prerequisite for checkpoint therapy. OncoImmunology *6*, e1294299. https://doi.org/10.1080/2162402X.2017.1294299.

18. Kuang, D.-M., Zhao, Q., Peng, C., Xu, J., Zhang, J.-P., Wu, C., and Zheng, L. (2009). Activated monocytes in peritumoral stroma of hepatocellular carcinoma foster immune privilege and disease progression through PD-L1. J. Exp. Med. *206*, 1327–1337. https://doi.org/10.1084/jem.20082173.

19. Tang, H., Liang, Y., Anders, R.A., Taube, J.M., Qiu, X., Mulgaonkar, A., Liu, X., Harrington, S.M., Guo, J., Xin, Y., et al. (2018). PD-L1 on host cells is essential for PD-L1 blockade–mediated tumor regression. J. Clin. Invest. *128*, 580–588. https://doi.org/10.1172/JCI96061.

20. Zhao, Y., Lee, C.K., Lin, C.-H., Gassen, R.B., Xu, X., Huang, Z., Xiao, C., Bonorino, C., Lu, L.-F., Bui, J.D., and Hui, E. (2019). PD-L1:CD80 Cis-Heterodimer Triggers the Co-stimulatory Receptor CD28 While Repressing the Inhibitory PD-1 and CTLA-4 Pathways. Immunity *51*, 1059–1073.e9. https://doi.org/10.1016/j.immuni.2019.11.003.

21. Chaudhri, A., Xiao, Y., Klee, A.N., Wang, X., Zhu, B., and Freeman, G.J. (2018). PD-L1 binds to B7-1 only in cis on the same cell surface. Cancer Immunol. Res. *6*, 921–929. https://doi.org/10.1158/2326-6066.CIR-17-0316.

22. Butte, M.J., Keir, M.E., Phamduy, T.B., Sharpe, A.H., and Freeman, G.J. (2007). Programmed Death-1 Ligand 1 Interacts Specifically with the B7-1 Costimulatory Molecule to Inhibit T Cell Responses. Immunity *27*, 111–122. https://doi.org/10.1016/j.immuni.2007.05.016.

23. Shin, D.S., and Ribas, A. (2015). The evolution of checkpoint blockade as a cancer therapy: what's here, what's next? Curr. Opin. Immunol. *33*, 23–35. https://doi.org/10.1016/j.coi.2015.01.006.

24. Márquez-Rodas, I., Cerezuela, P., Soria, A., Berrocal, A., Riso, A., González-Cao, M., and Martín-Algarra, S. (2015). Immune checkpoint inhibitors: therapeutic advances in melanoma. Ann. Transl. Med. *3*, 267. https://doi.org/10.3978/j.issn.2305-5839.2015.10.27.

25. Hughes, P.E., Caenepeel, S., and Wu, L.C. (2016). Targeted Therapy and Checkpoint Immunotherapy Combinations for the Treatment of Cancer. Trends Immunol. *37*, 462–476. https://doi.org/10.1016/j.it.2016.04.010.

26. Lee, H.T., Lee, J.Y., Lim, H., Lee, S.H., Moon, Y.J., Pyo, H.J., Ryu, S.E., Shin, W., and Heo, Y.-S. (2017). Molecular mechanism of PD-1/PD-L1 blockade via anti-PD-L1 antibodies atezolizumab and durvalumab. Sci. Rep. *7*, 5532. https://doi.org/10.1038/s41598-017-06002-8.

27. Liu, K., Tan, S., Chai, Y., Chen, D., Song, H., Zhang, C.W.-H., Shi, Y., Liu, J., Tan, W., Lyu, J., et al. (2017). Structural basis of anti-PD-L1 monoclonal antibody avelumab for tumor therapy. Cell Res. *27*, 151–153. https://doi.org/10.1038/cr.2016.102.

28. Ding, X., Gu, W., Zhong, Y., Hao, X., Liu, J., Xia, S., Luo, L., Chen, M., and Zhang, C. (2020). A novel HER2-targeting antibody 5G9 identified by large-scale trastuzumab-based screening exhibits potent synergistic antitumor activity. EBioMedicine *60*, 102996. https://doi.org/10.1016/j.ebiom.2020.102996.

29. Friedman, L.M., Rinon, A., Schechter, B., Lyass, L., Lavi, S., Bacus, S.S., Sela, M., and Yarden, Y. (2005). Synergistic down-regulation of receptor tyrosine kinases by combinations of mAbs: Implications for cancer immunotherapy. Proc. Natl. Acad. Sci. USA *102*, 1915–1920. https://doi.org/10.1073/pnas.0409610102.

30. Pedersen, M.W., Jacobsen, H.J., Koefoed, K., Hey, A., Pyke, C., Haurum, J.S., and Kragh, M. (2010). Sym004: a novel synergistic anti-epidermal growth factor receptor antibody mixture with superior anticancer efficacy. Cancer Res. *70*, 588–597. https://doi.org/10.1158/0008-5472.CAN-09-1417.

31. Spangler, J.B., Manzari, M.T., Rosalia, E.K., Chen, T.F., and Wittrup, K.D. (2012). Triepitopic antibody fusions inhibit cetuximab-resistant BRAF- and KRAS-mutant tumors via EGFR signal repression. J. Mol. Biol. *422*, 532–544. https://doi.org/10.1016/j.jmb.2012.06.014.

32. Kast, F., Schwill, M., Stüber, J.C., Pfundstein, S., Nagy-Davidescu, G., Rodríguez, J.M.M., Seehusen, F., Richter, C.P., Honegger, A., Hartmann, K.P., et al. (2021). Engineering an anti-HER2 biparatopic antibody with a multimodal mechanism of action. Nat. Commun. *12*, 3790. https://doi.org/10.1038/s41467-021-23948-6.

33. Cheng, J., Liang, M., Carvalho, M.F., Tigue, N., Faggioni, R., Roskos, L.K., and Vainshtein, I. (2020). Molecular Mechanism of HER2 Rapid Internalization and Redirected Trafficking Induced by Anti-HER2

Biparatopic Antibody. Antibodies *9*, 49. https://doi.org/10.3390/antib9030049.

34. DaSilva, J.O., Yang, K., Perez Bay, A.E., Andreev, J., Ngoi, P., Pyles, E., Franklin, M.C., Dudgeon, D., Rafique, A., Dore, A., et al. (2020). A Biparatopic Antibody That Modulates MET Trafficking Exhibits Enhanced Efficacy Compared with Parental Antibodies in MET-Driven Tumor Models. Clin. Cancer Res. *26*, 1408–1419. https://doi.org/10.1158/1078-0432.CCR-19-2428.
35. Geoghegan, J.C., Diedrich, G., Lu, X., Rosenthal, K., Sachsenmeier, K.F., Wu, H., Dall'Acqua, W.F., and Damschroder, M.M. (2016). Inhibition of CD73 AMP hydrolysis by a therapeutic antibody with a dual, non-competitive mechanism of action. mAbs *8*, 454–467. https://doi.org/10.1080/19420862.2016.1143182.
36. Stefano, J.E., Lord, D.M., Zhou, Y., Jaworski, J., Hopke, J., Travaline, T., Zhang, N., Wong, K., Lennon, A., He, T., et al. (2020). A highly potent CD73 biparatopic antibody blocks organization of the enzyme active site through dual mechanisms. J. Biol. Chem. *295*, 18379–18389. https://doi.org/10.1074/jbc.RA120.012395.
37. Benedetti, F., Stadlbauer, K., Stadlmayr, G., Rüker, F., and Wozniak-Knopp, G. (2021). A Tetravalent Biparatopic Antibody Causes Strong HER2 Internalization and Inhibits Cellular Proliferation. Life *11*, 1157. https://doi.org/10.3390/life11111157.
38. Moody, P.R., Sayers, E.J., Magnusson, J.P., Alexander, C., Borri, P., Watson, P., and Jones, A.T. (2015). Receptor Crosslinking: A General Method to Trigger Internalization and Lysosomal Targeting of Therapeutic Receptor:Ligand Complexes. Mol. Ther. *23*, 1888–1898. https://doi.org/10.1038/mt.2015.178.
39. Park, J.-J., Thi, E.P., Carpio, V.H., Bi, Y., Cole, A.G., Dorsey, B.D., Fan, K., Harasym, T., Iott, C.L., Kadhim, S., et al. (2021). Checkpoint inhibition through small molecule-induced internalization of programmed death-ligand 1. Nat. Commun. *12*, 1222. https://doi.org/10.1038/s41467-021-21410-1.
40. Zhang, Y., Du, X., Liu, M., Tang, F., Zhang, P., Ai, C., Fields, J.K., Sundberg, E.J., Latinovic, O.S., Devenport, M., et al. (2019). Hijacking antibody-induced CTLA-4 lysosomal degradation for safer and more effective cancer immunotherapy. Cell Res. *29*, 609–627. https://doi.org/10.1038/s41422-019-0184-1.
41. Kelly, R.L., Le, D., Zhao, J., and Wittrup, K.D. (2018). Reduction of nonspecificity motifs in synthetic antibody libraries. J. Mol. Biol. *430*, 119–130. https://doi.org/10.1016/j.jmb.2017.11.008.
42. Boder, E.T., and Wittrup, K.D. (1997). Yeast surface display for screening combinatorial polypeptide libraries. Nat. Biotechnol. *15*, 553–557. https://doi.org/10.1038/nbt0697-553.
43. Chao, G., Lau, W.L., Hackel, B.J., Sazinsky, S.L., Lippow, S.M., and Wittrup, K.D. (2006). Isolating and engineering human antibodies using yeast surface display. Nat. Protoc. *1*, 755–768. https://doi.org/10.1038/nprot.2006.94.
44. Müller, M.R., O'Dwyer, R., Kovaleva, M., Rudkin, F., Dooley, H., and Barelle, C.J. (2012). Generation and isolation of target-specific single-domain antibodies from shark immune repertoires. Methods Mol. Biol. *907*, 177–194. https://doi.org/10.1007/978-1-61779-974-7_9.
45. Honorato, R.V., Koukos, P.I., Jiménez-García, B., Tsaregorodtsev, A., Verlato, M., Giachetti, A., Rosato, A., and Bonvin, A.M.J.J. (2021). Structural Biology in the Clouds: The WeNMR-EOSC Ecosystem. Front. Mol. Biosci. *8*, 729513.
46. Zak, K.M., Kitel, R., Przetocka, S., Golik, P., Guzik, K., Musielak, B., Dömling, A., Dubin, G., and Holak, T.A. (2015). Structure of the Complex of Human Programmed Death 1, PD-1, and Its Ligand PD-L1. Structure *23*, 2341–2348. https://doi.org/10.1016/j.str.2015.09.010.
47. Krissinel, E., and Henrick, K. (2007). Inference of macromolecular assemblies from crystalline state. J. Mol. Biol. *372*, 774–797. https://doi.org/10.1016/j.jmb.2007.05.022.
48. The PyMOL Molecular Graphics System https://pymol.sourceforge.net/overview/index.htm.
49. Ridgway, J.B., Presta, L.G., and Carter, P. (1996). "Knobs-into-holes" engineering of antibody CH3 domains for heavy chain heterodimerization. Protein Eng. *9*, 617–621.
50. Merchant, A.M., Zhu, Z., Yuan, J.Q., Goddard, A., Adams, C.W., Presta, L.G., and Carter, P. (1998). An efficient route to human bispecific IgG. Nat. Biotechnol. *16*, 677–681. https://doi.org/10.1038/nbt0798-677.
51. Koerber, J.T., Hornsby, M.J., and Wells, J.A. (2015). An improved single-chain Fab platform for efficient display and recombinant expression. J. Mol. Biol. *427*, 576–586. https://doi.org/10.1016/j.jmb.2014.11.017.
52. Almagro, J.C., Daniels-Wells, T.R., Perez-Tapia, S.M., and Penichet, M.L. (2017). Progress and Challenges in the Design and Clinical Development of Antibodies for Cancer Therapy. Front. Immunol. *8*, 1751. https://doi.org/10.3389/fimmu.2017.01751.
53. Cox, A.L., Netski, D.M., Mosbruger, T., Sherman, S.G., Strathdee, S., Ompad, D., Vlahov, D., Chien, D., Shyamala, V., Ray, S.C., and Thomas, D.L. (2005). Prospective evaluation of community-acquired acute-phase hepatitis C virus infection. Clin. Infect. Dis. *40*, 951–958. https://doi.org/10.1086/428578.
54. Kumar, D., Mishra, A., Lisok, A., Kureshi, R., Shelake, S., Plyku, D., Sen, R., Doucet, M., De Silva, R.A., Mease, R.C., et al. (2021). Pharmacodynamic measures within tumors expose differential activity of PD(L)-1 antibody therapeutics. Proc. Natl. Acad. Sci. USA *118*, e2107982118. https://doi.org/10.1073/pnas.2107982118.
55. Spangler, J.B., Neil, J.R., Abramovitch, S., Yarden, Y., White, F.M., Lauffenburger, D.A., and Wittrup, K.D. (2010). Combination antibody treatment down-regulates epidermal growth factor receptor by inhibiting endosomal recycling. Proc. Natl. Acad. Sci. USA *107*, 13252–13257. https://doi.org/10.1073/pnas.0913476107.
56. Li, J.Y., Perry, S.R., Muniz-Medina, V., Wang, X., Wetzel, L.K., Rebelatto, M.C., Hinrichs, M.J.M., Bezabeh, B.Z., Fleming, R.L., Dimasi, N., et al. (2016). A Biparatopic HER2-Targeting Antibody-Drug Conjugate Induces Tumor Regression in Primary Models Refractory to or Ineligible for HER2-Targeted Therapy. Cancer Cell *29*, 117–129. https://doi.org/10.1016/j.ccell.2015.12.008.
57. Burr, M.L., Sparbier, C.E., Chan, Y.-C., Williamson, J.C., Woods, K., Beavis, P.A., Lam, E.Y.N., Henderson, M.A., Bell, C.C., Stolzenburg, S., et al. (2017). CMTM6 maintains the expression of PD-L1 and regulates anti-tumour immunity. Nature *549*, 101–105. https://doi.org/10.1038/nature23643.
58. Boyerinas, B., Jochems, C., Fantini, M., Heery, C.R., Gulley, J.L., Tsang, K.Y., and Schlom, J. (2015). Antibody-dependent cellular cytotoxicity (ADCC) activity of a novel anti-PD-L1 antibody avelumab (MSB0010718C) on human tumor cells. Cancer Immunol. Res. *3*, 1148–1157. https://doi.org/10.1158/2326-6066.CIR-15-0059.
59. Juliá, E.P., Amante, A., Pampena, M.B., Mordoh, J., and Levy, E.M. (2018). Avelumab, an IgG1 anti-PD-L1 Immune Checkpoint Inhibitor, Triggers NK Cell-Mediated Cytotoxicity and Cytokine Production Against Triple Negative Breast Cancer Cells. Front. Immunol. *9*, 2140. https://doi.org/10.3389/fimmu.2018.02140.
60. Cotton, A.D., Nguyen, D.P., Gramespacher, J.A., Seiple, I.B., and Wells, J.A. (2021). Development of Antibody-Based PROTACs for the Degradation of the Cell-Surface Immune Checkpoint Protein PD-L1. J. Am. Chem. Soc. *143*, 593–598. https://doi.org/10.1021/jacs.0c10008.
61. Banik, S.M., Pedram, K., Wisnovsky, S., Ahn, G., Riley, N.M., and Bertozzi, C.R. (2020). Lysosome-targeting chimaeras for degradation of extracellular proteins. Nature *584*, 291–297. https://doi.org/10.1038/s41586-020-2545-9.
62. Polakis, P. (2016). Antibody Drug Conjugates for Cancer Therapy. Pharmacol. Rev. *68*, 3–19. https://doi.org/10.1124/pr.114.009373.
63. Thurber, G.M., Schmidt, M.M., and Wittrup, K.D. (2008). Antibody tumor penetration: Transport opposed by systemic and antigen-mediated clearance. Adv. Drug Deliv. Rev. *60*, 1421–1434. https://doi.org/10.1016/j.addr.2008.04.012.
64. Nessler, I., Khera, E., Vance, S., Kopp, A., Qiu, Q., Keating, T.A., Abu-Yousif, A.O., Sandal, T., Legg, J., Thompson, L., et al. (2020). Increased

Tumor Penetration of Single-Domain Antibody–Drug Conjugates Improves *In Vivo* Efficacy in Prostate Cancer Models. Cancer Res. *80*, 1268–1278. https://doi.org/10.1158/0008-5472.CAN-19-2295.

65. Rumfelt, L.L., McKINNEY, E.C., Taylor, E., and Flajnik, M.F. (2002). The Development of Primary and Secondary Lymphoid Tissues in the Nurse Shark *Ginglymostoma cirratum* : B-Cell Zones Precede Dendritic Cell Immigration and T-Cell Zone Formation During Ontogeny of the Spleen. Scand. J. Immunol. *56*, 130–148. https://doi.org/10.1046/j.1365-3083.2002.01116.x.
66. Schindelin, J., Arganda-Carreras, I., Frise, E., Kaynig, V., Longair, M., Pietzsch, T., Preibisch, S., Rueden, C., Saalfeld, S., Schmid, B., et al. (2012). Fiji: an open-source platform for biological-image analysis. Nat. Methods *9*, 676–682. https://doi.org/10.1038/nmeth.2019.
67. Wester, M.J., Schodt, D.J., Mazloom-Farsibaf, H., Fazel, M., Pallikkuth, S., and Lidke, K.A. (2021). Robust, fiducial-free drift correction for super-resolution imaging. Sci. Rep. *11*, 23672. https://doi.org/10.1038/s41598-021-02850-7.
68. Schodt, D.J., Wester, M.J., Fazel, M., Khan, S., Mazloom-Farsibaf, H., Pallikkuth, S., Meddens, M.B.M., Farzam, F., Burns, E.A., Kanagy, W.K., et al. (2023). SMITE: Single Molecule Imaging Toolbox Extraordinaire (MATLAB). J. Open Source Softw *8*, 5563. https://doi.org/10.21105/joss.05563.
69. Smith, C.S., Joseph, N., Rieger, B., and Lidke, K.A. (2010). Fast, single-molecule localization that achieves theoretically minimum uncertainty. Nat. Methods *7*, 373–375. https://doi.org/10.1038/nmeth.1449.
70. Schodt, D.J., and Lidke, K.A. (2021). Spatiotemporal Clustering of Repeated Super-Resolution Localizations via Linear Assignment Problem. Front. Bioinform. *1*, 724325.
71. Ester, M., Kriegel, H., Sander, J., and Xu, X. (1996). A Density-Based Algorithm for Discovering Clusters in Large Spatial Databases with Noise (AAAI Press), pp. 226–231.
72. Massey, F.J. (1951). The Kolmogorov-Smirnov Test for Goodness of Fit. J. Am. Stat. Assoc. *46*, 68–78. https://doi.org/10.2307/2280095.
73. Rutebemberwa, A., Ray, S.C., Astemborski, J., Levine, J., Liu, L., Dowd, K.A., Clute, S., Wang, C., Korman, A., Sette, A., et al. (2008). High Programmed Death-1 levels on HCV specific T cells during acute infection are associated with viral persistence and require preservation of cognate antigen during chronic infection. J. Immunol. *181*, 8215–8225.
74. Page, K., Melia, M.T., Veenhuis, R.T., Winter, M., Rousseau, K.E., Massaccesi, G., Osburn, W.O., Forman, M., Thomas, E., Thornton, K., et al. (2021). Randomized Trial of a Vaccine Regimen to Prevent Chronic HCV Infection. N. Engl. J. Med. *384*, 541–549. https://doi.org/10.1056/NEJMoa2023345.
75. Cox, A.L., Mosbruger, T., Mao, Q., Liu, Z., Wang, X.-H., Yang, H.-C., Sidney, J., Sette, A., Pardoll, D., Thomas, D.L., and Ray, S.C. (2005). Cellular immune selection with hepatitis C virus persistence in humans. J. Exp. Med. *201*, 1741–1752. https://doi.org/10.1084/jem.20050121.

STAR★METHODS

KEY RESOURCES TABLE

REAGENT or RESOURCE	SOURCE	IDENTIFIER
Antibodies		
Mouse monoclonal anti-nurse shark IgNAR (clone GA8)	Absolute Antibody; Rumfelt et al.[65]	Cat# Ab01553-2.0
Sheep polyclonal anti-mouse IgG (whole molecule) horseradish peroxidase	Sigma-Aldrich	Cat# A6782; RRID: AB_258315
Mouse monoclonal anti-human IgG Fc APC (clone HP6017)	BioLegend	Cat# 409306; RRID: AB_11149491
Mouse monoclonal anti-myc epitope Alexa Fluor 647 (clone 9B11)	Cell Signaling Technologies	Cat# 2233; RRID: AB_823474
Mouse monoclonal anti-human CD274 (B7-H1, PD-L1) PE (clone MIH2)	BioLegend	Cat# 393607; RRID: AB_2749924
Rabbit polyclonal anti-Alexa Fluor 488	ThermoFisher Scientific	Cat# A-11094; RRID: AB_221544
Rabbit monoclonal anti-human EEA1 (clone F.43.1)	ThermoFisher Scientific	Cat# MA5-14794; RRID: AB_10985824
Mouse monoclonal anti-human CD107A AlexaFluor 647(clone H4A3)	BD Biosciences	Cat# 562622; RRID: AB_2737684
Goat polyclonal anti-rabbit IgG (H+L) AlexaFluor 568	ThermoFisher Scientific	Cat# A-11011; RRID: AB_143157
Mouse monoclonal ant-human IFN-γ (clone 1-D1K)	MAbtech	Cat# 3420-3-250; RRID: AB_907283
Mouse monoclonal biotin-labeled anti-human IFN-γ (clone 7-B6-1)	MAbtech	Cat# 3420-6-250, RRID: AB_907273
Bacterial and virus strains		
One Shot™ MAX Efficiency™ DH5α-T1R Competent Cells	ThermoFisher Scientific	Cat# 12297016
Biological samples		
Human Peripheral blood mononuclear cells	Cox et al.[53]	N/A
Chemicals, peptides, and recombinant proteins		
OptiPRO™ SFM	ThermoFisher Scientific	Cat# 12309019
FreeStyle™ 293 Expression Medium	ThermoFisher Scientific	Cat# 12338018
Polyethylenimine, Linear, MW 25000, Transfection Grade (PEI 25K™)	Polysciences	Cat# 23966
4% paraformaldehyde in 0.1M PBS, pH7.4	Electron Microscopy Sciences	Cat# 15735-85
Alexa Flour 647-conjugated streptavidin	ThermoFisher Scientific	Cat# S21374
Monensin sodium salt	Sigma-Aldrich	Cat# M5273; CAS: 22373-78-0
Glucose oxidase, Type VII	Sigma-Aldrich	Cat# G2133; Cas: RN 9001-37-0
Catalase	Sigma-Aldrich	Cat# C9322; Cas: 9001-05-2
[^{18}F]DK222 Peptide	Kumar et al.[54]	N/A
Human PD-L1 ECD	This paper	N/A
Mouse PD-L1 ECD	This paper	N/A
Biotinylated human PD-L1 ECD	This paper	N/A
PD-1	This paper	N/A
HCV peptides (CINGVCWTV)	Genemed Synthesis	N/A
IRDye® 800CW NHS Ester	LI-COR Biosciences	Cat# 929-70021
Soluble Atezolizumab scFv	This paper	N/A
Soluble D12 scFv	This paper	N/A

(*Continued on next page*)

Continued

REAGENT or RESOURCE	SOURCE	IDENTIFIER
Soluble A9 VNAR	This paper	N/A
Soluble B8 VNAR	This paper	N/A
Atezolizumab (N297A)	This paper	N/A
D12 Ab (N297A)	This paper	N/A
A9 VNAR Fc (N297A)	This paper	N/A
B8 VNAR Fc (N297A)	This paper	N/A
BS1 (N297A)	This paper	N/A
BS14 (N297A)	This paper	N/A
BS20 (N297A)	This paper	N/A
BS7 (N297A)	This paper	N/A
BS22 (N297A)	This paper	N/A
BS24 (N297A)	This paper	N/A
BS23 (N297A)	This paper	N/A
BS21 (N297A)	This paper	N/A
BS12 (N297A)	This paper	N/A
BS15 (N297A)	This paper	N/A
BS19 (N297A)	This paper	N/A
BS16 (N297A)	This paper	N/A
BS8 (N297A)	This paper	N/A
TS1421 (N297A)	This paper	N/A
TS148 (N297A)	This paper	N/A
TS2320 (N297A)	This paper	N/A
TS1912 (N297A)	This paper	N/A
TS1012 (N297A)	This paper	N/A
TS1621 (N297A)	This paper	N/A
TS1624 (N297A)	This paper	N/A
TS1521 (N297A)	This paper	N/A
TS2319 (N297A)	This paper	N/A
TS238 (N297A)	This paper	N/A
Critical commercial assays		
BirA Biotin-Protein Ligase Standard Reaction Kit	Avidity LLC	Cat# BirA500
Octet® Streptavidin (SA) Biosensor	Sartorius	Cat# 18-5019
FastGene Scriptase II	Bulldog Bio	Cat# LS53
Phusion polymerase	New England Biolabs	Cat# M0530S
Alexa Fluor™ 488 Microscale Protein Labeling Kit	ThermoFisher Scientific	Cat# A30006
pHrodo™ iFL Green Microscale Protein Labeling Kit	ThermoFisher Scientific	Cat# P36015
PD-1/PD-L1 Blockade Bioassay Kit	Promega	Cat# J1250
Experimental models: Cell lines		
Freestyle™ 293-F cells	ThermoFisher Scientific	Cat# R79007; RRID: CVCL_6642
Jurkat cells expressing human PD-1 and cognate TCR	Promega	Cat# J1250
CHO-K1 cells expressing PD-L1 and a T-cell-activating surface protein (antigen-presenting cells, APCs)	Promega	Cat# J1250
Human: MDA-MB-231 cells	ATCC	Cat# HTB-26; RRID: CVCL_0062
Human: H2444 cells	ATCC	Cat# CRL-5945; RRID: CVCL_1552
Human: HCC38 cells	ATCC	Cat# CRL-2314; RRID: CVCL_1267
Human: H226 cells	ATCC	Cat# CRL-5826; RRID: CVCL_1544
Human: A549 cells	ATCC	Cat# CCL-185; RRID: CVCL_0023

(*Continued on next page*)

Continued

REAGENT or RESOURCE	SOURCE	IDENTIFIER
Chinese hamster ovary (CHO)-K1 cells stably transduced with PD-L1	Kumar et al.[54]	N/A
Experimental models: Organisms/strains		
Mouse: NOD.Cg-Prkdcscid Il2rgtm1Wjl/SzJ (NSG™)	The Jackson Laboratory	Strain #:005557; RRID: IMSR_JAX:005557
Recombinant DNA		
Human IgG1 constant heavy chain sequence	ImMunoGeneTics (IMGT)	IMGT: JN582178
Human IgG1 constant lambda chain sequence	ImMunoGeneTics (IMGT)	IMGT: J00241
Atezolizumab VH (1-118) and VL (1-107) sequences	Drugbank	Drugbank: DB11595
pCT3CBN	Derived from pCTcon2 (Boder and Wittrup, 1997b)	N/A
pCT3CBN_ Atezolizumab_scFv	This paper	N/A
pCT3CBN_A1_scFv	This paper	N/A
pCT3CBN_B5_scFv	This paper	N/A
pCT3CBN_B6_scFv	This paper	N/A
pCT3CBN_B7_scFv	This paper	N/A
pCT3CBN_B8_scFv	This paper	N/A
pCT3CBN_C7_scFv	This paper	N/A
pCT3CBN_D2_scFv	This paper	N/A
pCT3CBN_D8_scFv	This paper	N/A
pCT3CBN_D12_scFv	This paper	N/A
pCT3CBN_A9_VNAR	This paper	N/A
pCT3CBN_B8_VNAR	This paper	N/A
pCT3CBN_B11_VNAR	This paper	N/A
pCT3CBN_C7_VNAR	This paper	N/A
pCT3CBN_C4_VNAR	This paper	N/A
gWiz High Expression Blank Vector	Genlantis	Ca# P000200
gWiz_Human_PD-L1_ECD (PD-L1 sequence obtained from UniProt: Q9NZQ7)	This paper	N/A
gWiz_Mouse_PD-L1_ECD (PD-L1 sequence obtained from UniProt: Q9EP73)	This paper	N/A
gWiz_human_PD-1 (PD-1 sequence obtained from Uniprot: Q15116)	This paper	N/A
gWiz_Atezolizumab_scFv	This paper	N/A
gWiz_D12_scFv	This paper	N/A
gWiz_B8_VNAR	This paper	N/A
gWiz_A9_VNAR	This paper	N/A
gWiz_Atezolizumab_HC_N297A	This paper	N/A
gWiz_Atezolizumab_LC	This paper	N/A
gWiz_D12_HC_N297A	This paper	N/A
gWiz_D12_LC	This paper	N/A
gWiz_A9_Fc_N297A	This paper	N/A
gWiz_B8_Fc_N297A	This paper	N/A
gWiz_BS1_Knobs_N297A	This paper	N/A
gWiz_BS1_Holes_N297A	This paper	N/A
gWiz_BS14_HC_N297A	This paper	N/A
gWiz_BS14_LC (same as gWiz_Atezolizumab_LC)	This paper	N/A
gWiz_BS20_HC_N297A (same as gWiz_Atezolizumab_HC_N297A)	This paper	N/A

(*Continued on next page*)

Continued

REAGENT or RESOURCE	SOURCE	IDENTIFIER
gWiz_BS20_LC	This paper	N/A
gWiz_BS7_HC_N297A (same as gWiz_Atezolizumab_HC_N297A)	This paper	N/A
gWiz_BS7_LC	This paper	N/A
gWiz_BS22_HC_N297A	This paper	N/A
gWiz_BS22_LC (same as gWiz_Atezolizumab_LC)	This paper	N/A
gWiz_BS24_HC_N297A (same as gWiz_Atezolizumab_HC_N297A)	This paper	N/A
gWiz_BS24_LC	This paper	N/A
gWiz_BS23_HC_N297A	This paper	N/A
gWiz_BS23_LC (same as gWiz_Atezolizumab_LC)	This paper	N/A
gWiz_BS21_HC_N297A (same as gWiz_Atezolizumab_HC_N297A)	This paper	N/A
gWiz_BS21_LC	This paper	N/A
gWiz_BS12_Knobs_N297A	This paper	N/A
gWiz_BS12_Holes_N297A	This paper	N/A
gWiz_BS15_HC_N297A	This paper	N/A
gWiz_BS15_LC (same as gWiz_Atezolizumab_LC)	This paper	N/A
gWiz_BS19_HC_N297A (same as gWiz_Atezolizumab_HC_N297A)	This paper	N/A
gWiz_BS19_LC	This paper	N/A
gWiz_BS16_HC_N297A	This paper	N/A
gWiz_BS16_LC (same as gWiz_Atezolizumab_LC)	This paper	N/A
gWiz_BS8_HC_N297A (same as gWiz_Atezolizumab_HC_N297A)	This paper	N/A
gWiz_BS8_LC	This paper	N/A
gWiz_TS1421_HC_N297A (same as gWiz_BS14_HC_N297A)	This paper	N/A
gWiz_TS1421_LC (same as gWiz_BS21_LC)	This paper	N/A
gWiz_TS148_HC_N297A (same as gWiz_BS14_HC_N297A)	This paper	N/A
gWiz_TS148_LC (same as gWiz_BS8_LC)	This paper	N/A
gWiz_TS2320_HC_N297A (same as gWiz_BS23_HC_N297A)	This paper	N/A
gWiz_TS2320_LC (same as gWiz_BS20_LC)	This paper	N/A
gWiz_TS1912_Knobs_N297A	This paper	N/A
gWiz_TS1912_Holes_N297A	This paper	N/A
gWiz_TS1012_Knobs_N297A	This paper	N/A
gWiz_TS1012_Holes_N297A	This paper	N/A
gWiz_TS1621_HC_N297A (same as gWiz_BS16_HC_N297A)	This paper	N/A
gWiz_TS1621_LC (same as gWiz_BS21_LC)	This paper	N/A
gWiz_TS1624_HC_N297A (same as gWiz_BS16_HC_N297A)	This paper	N/A
gWiz_TS1624_LC (same as gWiz_BS24_LC)	This paper	N/A
gWiz_TS1521_HC_N297A (same as gWiz_BS15_HC_N297A)	This paper	N/A
gWiz_TS1521_LC (same as gWiz_BS21_LC)	This paper	N/A

(*Continued on next page*)

Continued

REAGENT or RESOURCE	SOURCE	IDENTIFIER
gWiz_TS2319_HC_N297A (same as gWiz_BS23_HC_N297A)	This paper	N/A
gWiz_TS2319_LC (same as gWiz_BS19_LC)	This paper	N/A
gWiz_TS238_HC_N297A (same as gWiz_BS23_HC_N297A)	This paper	N/A
gWiz_TS238_LC (same as gWiz_BS8_LC)	This paper	N/A
Software and algorithms		
GraphPad Prism v9.3.1	GraphPad	https://www.graphpad.com/
FlowJo v10.7.1	FlowJo, LLC	https://www.flowjo.com/solutions/flowjo
PyMOL v2.3.2	PyMOL	https://pymol.org/2/
BioRender	BioRender	https://biorender.com/
UNICORN™ v7.1	Cytiva Life Sciences	https://www.cytivalifesciences.com/en/us/shop/chromatography/software/unicorn-7-p-05649
Octet® Data Analysis software v7.1	FortéBio	N/A
Fiji	ImageJ; Schindelin et al.[66]	https://imagej.net/software/fiji/
MATLAB R2018b	MathWorks	https://www.mathworks.com/products/matlab.html
Single Molecule Imaging Toolbox Extraordinare (SMITE)	Schodt et al.[68]	https://github.com/LidkeLab/smite
High Ambiguity Driven Protein-Protein Docking v2.4	Honorato et al.[45]	https://wenmr.science.uu.nl/haddock2.4/
Proteins, Interfaces, Structures, and Assemblies (PISA) service	Krissinel et al.[47]	https://www.ebi.ac.uk/pdbe/pisa/
Pearl Impulse Software v2.0	LI-COR Biosciences	N/A
Other		
Ni-NTA Affinity Resin	Abcam	Cat# ab270549
Pierce™ Protein G Agarose	ThermoFisher Scientific	Cat# 20397
Streptavidin MicroBeads	Miltenyi Biotec	Cat# 130-048-101
Anti-Alexa Fluor 647 MicroBeads	Miltenyi Biotec	Cat# 130-091-395
Quantum™ Simply Cellular® anti-mouse IgG beads	Bangs Laboratories	Cat# 815

RESOURCE AVAILABILITY

Lead contact

Further information and requests for resources and reagents should be directed to and will be fulfilled by the lead contact, Jamie B. Spangler (jamie.spangler@jhu.edu).

Materials availability

Reagents generated in this study will be made available on request, but we may require a completed Materials Transfer Agreement.

Data and code availability

- All data reported in this paper will be shared by the lead contact upon request.
- This paper does not report original code.
- Any additional information required to reanalyze the data reported in this paper is available from the lead contact upon request.

EXPERIMENTAL MODEL AND STUDY PARTICIPANT DETAILS

Cell lines

MDA-MB-231 cells (ATCC) were cultured in Dulbecco's Modified Eagle Medium (DMEM) supplemented with 10% fetal bovine serum (FBS), 2 mM L-glutamine, 1 mM Pyruvate, and penicillin-streptomycin (100 μg/mL) (Thermo Fisher Scientific). H2444 cells (ATCC), HCC38 cells (ATCC) and H226 cells (ATCC) were cultured in RPMI-1640 medium supplemented with 10% FBS and

penicillin-streptomycin (100 μg/mL). Chinese hamster ovary (CHO)-K1 cells (ATCC) stably transduced with PD-L1 were kindly provided to us by Dr. Sridhar Nimmagadda (Department of Oncology at Johns Hopkins Medicine) and cultured in F-12K medium containing 10% FBS, 2 mM L-glutamine, 2 mg/mL. PD-L1 expression was confirmed regularly by flow cytometry. G418 Sulfate (Thermo Fisher Scientific), and penicillin-streptomycin (100 μg/mL). A549 cells (ATCC) and CHO-K1 cells (Promega) were cultured in F-12K medium containing 10% FBS and penicillin streptomycin (100 μg/mL). Jurkat cells (Promega) were cultured in RPMI-1640 medium supplemented with 10% FBS and penicillin-streptomycin (100 μg/mL). Human embryonic kidney (HEK) 293F cells (Thermo Life Technologies) were cultured in FreeStyle 293 Expression Medium (Thermo Fisher Scientific) containing penicillin-streptomycin (2 μg/mL). All cells were grown at 37°C and 5% CO_2. HEK 293F cells were rotated continuously at 125 rpm. Cell lines were validated by commercial vendors.

Human PBMCs

Blood samples were obtained from subjects enrolled in the BBAASH cohort.[53] As previously described, this study included consenting males and females aged 15-30 years who were hepatitis C virus (HCV) antibody negative and acknowledged use of injection drugs. Participants who consented to co-enroll in a substudy of acute-phase HCV infection had blood samples obtained for isolation of serum, plasma, and peripheral blood mononuclear cells in a protocol designed for monthly follow-up. At each visit, participants were provided counseling to reduce the risks of injection drug use. The study protocols were approved by the institutional review boards of the Johns Hopkins Schools of Medicine and Hygiene and Public Health.[53] Human peripheral blood mononuclear cells (PBMCs) were isolated from whole blood by density gradient centrifugation using a Ficoll-Hypaque (Ficoll Paque, MilliporeSigma), according to the manufacturer's protocol.

Mice

NSG mice (The Jackson Laboratories, Strain # 005557) were obtained from the Johns Hopkins University Immune Compromised Animal Core. For pharmacokinetic studies, 6 week-old female NSG mice (n = 4 mice per cohort) were used, and for biodistribution studies, 6 week-old female NSG mice (n=5 mice per cohort) Animals were housed in specific pathogen-free conditions and experiments conducted in accordance with the Johns Hopkins University Animal Care and Use Committee (ACUC) under protocol number MO20M285.

METHOD DETAILS

Protein expression and purification

The extracellular domain of human PD-L1 (amino acids 19-228), antibody fragments isolated from yeast surface display-based selections (scFvs and VNARs), and the heavy and light chains of monoclonal or multiparatopic human IgG1 antibodies were inserted into the gWiz mammalian expression vector (Genlantis). The sequence of atezolizumab was obtained through Drugbank. scFv constructs consisted of the variable heavy (V_H) chain followed by the variable light chain (V_L) separated by a $(G_4S)_3$ linker. For PD-L1, scFv, and VNAR constructs, a C-terminal biotin acceptor peptide (GLNDIFEAQKIEWHE) and 6× His-tag for purification were also included. HEK 293F cells were grown to 1.2×10^6 cells/mL and on the day of transfection were diluted to 1×10^6 cells/mL. Polyethyleneimine (PEI, Polysciences, 2 mg per Liter cells) and midiprepped DNA (1 mg total DNA per Liter cells) were separately diluted to 0.1 and 0.05 mg/mL, respectively, in OptiPro medium (Thermo Life Technologies), and incubated at room temperature for 15 min. For antibodies, optimal ratios of heavy and light chain constructs were mixed prior to dilution for co-transfection. Subsequently, PEI was added to an equal volume of DNA and incubated proceeded at room temperature for 15 min. The DNA/PEI mixture was then added to the HEK 293F cells at 40 mL/L and incubated for 72-96 h. Proteins were harvested from HEK 293F cell supernatants by either Ni-NTA (Expedeon) affinity chromatography for 6× His-tagged molecules or Protein G (VWR) affinity chromatography for antibody constructs and multispecific antibody fusion proteins. Biotinylated proteins were prepared via overnight biotinylation at 4°C using BirA ligase enzyme in 0.5 mM Bicine pH 8.3, 100 mM ATP, 100 mM magnesium acetate, and 500 mM biotin (Avidity). Proteins were further purified using a Superdex 200 sizing column on a fast protein liquid chromatography (FPLC) instrument (GE Healthcare) equilibrated in either HEPES-buffered saline (HBS) or phosphate-buffered saline (PBS). Purity of post-FPLC proteins was verified by running analytical samples over the Superdex 200 sizing column a second time, ensuring that all proteins used in the study were free of aggregates and multimers. Fluorophore-labeled proteins were prepared by NHS-conjugation according to the manufacturer's instructions and SEC was conducted after fluorescent labelling to remove aggregates.

Protein stability tests

Purified TS1521 (1 mg/mL in HBS) was cryopreserved at −80°C for 3 days and then thawed prior to SEC analysis. The thawed protein was then incubated at 37°C for 0, 7, 14, or 21 days. At each time point, 500 μg TS1521 was analyzed by SEC using a Superdex 200 Increase 10/300 GL column (GE Healthcare) on an FPLC instrument, equilibrated in HBS.

Yeast surface binding studies

General yeast display protocols were carried out using EBY-100 yeast cells as described previously.[42,43] The variable heavy (V_H) chain followed by the variable light (V_L) chain of the anti-PD-L1 antibody atezolizumab, separated by a $(G_4S)_3$ linker, were cloned into the pCT3CBN yeast display vector. Other clones were selected from a naïve yeast-displayed scFv library.[41] Yeast were grown

overnight in SDCAA medium at 30°C and shaking at 200 rpm. Yeast were induced in SGCAA at an optical density (OD) of 1.0 (1×10^7 cells/mL) and grown for an additional 24-48 h at 20°C. After induction, 10^5 yeast per well were transferred to a 96-well plate and incubated in PBE (PBS with 0.1% bovine serum albumin [BSA] and 1 mM ethylenediaminetetraacetic acid [EDTA]) containing serial dilutions of biotinylated PD-L1 for 2 h at room temperature. Cells were then washed and incubated for an additional 20 min at 4°C with 50 nM Alexa Flour 647-conjugated streptavidin (SA-647, Thermo Fisher Scientific) in PBE. Cells were analyzed using a Beckman Coulter CytoFLEX flow cytometer. Data were analyzed in Prism software (GraphPad) using a single logistic model, and equilibrium dissociation constant (K_D) values were determined. Experiments were performed in triplicate and repeated twice with similar results.

Shark immunizations

Two juvenile nurse sharks (one male, one female, aged between 2-3 years and weighing between 2.0-2.9 kg), were held in a continuously-recirculating 12,000 L seawater tank maintained at 28°C, in the Aquaculture Research Center at the Institute of Marine & Environmental Technology (IMET), Baltimore, USA. The sharks were primed with an antigen cocktail containing 62.5 μg recombinant human PDL1 emulsified in complete Freund's adjuvant (CFA) and administered subcutaneously into the ventral surface of the lateral fin. At three-week intervals the sharks were boosted with 62.5 μg PDL1 emulsified in incomplete Freund's adjuvant (IFA) also administered subcutaneously into the opposite lateral fin, or intravenously with 50 μg (unadjuvanted) soluble PDL1 diluted in shark PBS and administered directly into the caudal sinus; each animal received four immunizations in total. A blood sample was drawn from the caudal vein two weeks after the final immunization, mixed with 1/10 volume of heparin (reconstituted to 1000 U/mL in shark-modified PBS), and centrifuged at 1000 rpm for 10 min to separate peripheral blood lymphocytes (PBLs) and blood plasma. Sharks were sedated with MS-222 prior to any procedure and all animal procedures were conducted in accordance with University of Maryland, School of Medicine Institutional Animal Care and Use Committee (IACUC) approved protocols.

IgNAR antigen-binding ELISAs

Antigen-binding ELISAs were performed on 96-well Nunc MaxiSorp flat bottom microtiter plates coated with 100 μL per well of 10 μg/mL recombinant human PDL1 for 1 h at room temperature and then blocked with 5% milk-PBS (MPBS) solution; control wells were not coated prior to blocking. Wells were washed 2-4 times with 200 μL/well PBS containing 0.5% Tween20 (PBST) after each step. Plasma was diluted 1:30 in PBS and a 1:3 serial dilution series set up on each plate. Samples of 100 μL/well were incubated for 2 h at room temperature. Nurse shark anti-IgNAR mouse monoclonal antibody GA8[65] was diluted 1:2 in PBS and 100 μL/well added to wells. Sheep anti-mouse IgG (whole molecule), peroxidase conjugate (Sigma Aldrich), diluted 1:1,000 in MPBS was then added at 100 μL/well. Plates were developed with 100 μL/well tetramethyl benzidine (TMB) substrate. After 5 mins the reaction was stopped by the addition of an equal volume of 1M H_2SO_4 and the absorbance of each well read at 450nm.

cDNA synthesis

PBLs were lysed in phenol solution and total RNA prepared from each as per standard protocols. Oligo-dT-primed cDNA was prepared for each animal using FastGene Scriptase II (Bulldog Bio) according to the manufacturer's instructions. Briefly, 1 μg of PBL total RNA was mixed with 1 μL of 80 μM oligo dT primer and 2 μL of dNTPs (2 mM each) in a 0.5 mL PCR tube, and the volume made up to 12.5 μL with molecular grade water. The mixture was heated to 65°C for 5 min on a PCR block then rapidly chilled on ice. After chilling, 4 μL of 5x FastGene Scriptase II buffer (Bulldog Bio) and 2 μL of 0.1 M DTT were added to the mixture and incubated at 42°C for 2 min. The mixture was again chilled on ice before the addition of 1 μL of FastGene Scriptase II enzyme (200 U/μl) (Bulldog Bio) and then incubated at 42°C for 50 min to permit cDNA synthesis. Finally, the mixture was heated to 70°C for 15 min to inactivate the reverse transcriptase enzyme.

VNAR library cloning

cDNA encoding the VNAR variable domain was PCR amplified using Phusion polymerase (New England Biolabs) according to the manufacturer's instructions, and the desired product isolated by gel electrophoresis. A second round of PCR amplification was performed using primers containing an additional 50 bp on both the 3' and 5' ends which overlapped with adjacent regions of the pCTcon2 yeast display vector. The pCtcon2 vector was prepared for homologous recombination by digestion with NheI and BamHI, and both the linearized vector and VNAR insert were transformed into EBY100 yeast by electroporation.

Yeast library selections

A previously described synthetic single-chain variable fragment (scFv) yeast library[41] was kindly provided by Dr. K. Dane Wittrup (Chemical Engineering and Biological Engineering, MIT). Selections were performed using magnetic-activated cell sorting (MACS) with LS MACS separation columns (Miltenyi Biotec), according to the manufacturer's protocol. The first round of selections was performed with 1×10^{10} cells to achieve 10-fold coverage of the naïve library, and subsequent rounds used 1×10^8 cells. All selections were carried out at 4°C. PD-L1 oligomer was formed by incubating 400 nM biotinylated PD-L1 with SA microbeads (Miltenyi Biotec) for 15 min. In applicable rounds, PD-L1 tetramer was formed by incubating a 4:1 ratio of biotinylated PD-L1 to SA-647 for 15 min. Each MACS selection was preceded by a negative selection in which yeast were incubated with either anti-Alexa Fluor 647 or SA-coated microbeads (Miltenyi Biotec), and clones non-specifically binding to the microbeads were discarded. Between each round, the selected yeast were regrown overnight in SDCAA and then induced in SGCAA for 48 h.

In the first round, yeast were incubated with 250 μL PD-L1 oligomer in 4.7 mL PBE for 2 h, followed by MACS selection. The second round was a myc-tag selection to isolated full-length antibodies, in which yeast were incubated with 1:100 v/v ratio of Alexa Fluor 647-conjugated anti-myc eptipope antibody (Cell Signaling Technologies) in PBE for 2 h, followed by a 15 min incubation with 50 μL anti-Alexa Fluor 647 microbeads in 950 μL PBE. In the third round, yeast were incubated with 50 nM PD-L1 tetramer for 2 h, followed by a 15 min incubation with 50 μL anti-Alexa Fluor 647 microbeads as in the second round. In the fourth round, the yeast were incubated with 2 μM biotinylated PD-L1 for 2 h, followed by a 10 min incubation with 1:200 v/v SA-647 and another 10 min incubation with anti-Alexa Fluor 647 microbeads. Yeast selected after the fourth round were plated and individual clones were picked for screening.

Bio-layer interferometry

Antibody binding and competition measurements were obtained using bio-layer interferometry (BLI) on an OctetRED96 instrument (Sartorius). For binding studies, biotinylated PD-L1 was immobilized to streptadvidin (SA)-coated biosensors (Sartorius) in 0.45 μm filtered PBSA (phosphate-buffered saline containing 0.1% BSA). Target proteins were serially diluted in PBSA. Binding kinetics were measured by submerging biosensors in these dilutions for 300 seconds (association), followed by submerging the biosensors in wells containing PBSA alone for 300 seconds (dissociation). Tips were regenerated in 0.1 M glycine pH 2.7. Curves were fitted using the Octet Data Analysis HT Software version 7.1 (Sartorius), assuming a 1:1 binding model to determine the association rates, dissociation rates, and K_D values. Experiments were repeated twice with similar results.

For competitive binding studies, biotinylated protein was immobilized to streptavidin (SA)-coated biosensors (Sartorius) in 0.45 μm filtered PBSA (phosphate-buffered saline containing 0.1% BSA). Competitor proteins were serially diluted into PBSA containing a saturating concentration of PD-L1 and incubated at room temperature for 30 min. Binding kinetics were measured by submerging biosensors in these mixtures for 300 seconds (association), and subsequently submerging the biosensors in wells containing only PBSA for 300 seconds (dissociation). Tips were regenerated in 0.1 M glycine pH 2.7. Extent of binding in presence of competitor antibody was determined by total response measured after 295 seconds. Signal was normalized to that of the PD-L1 only sample. Data were analyzed in Prism software (GraphPad) using a single logistic model, and half maximal inhibitory concentration (IC_{50}) values were determined where applicable. Experiments were repeated twice with similar results.

Quantification of target expression

The PD-L1 expression levels of MDA-MB-231, A549, HCC38, H226, H2444, and PD-L1-transduced CHO-K1 cells were quantified using Quantum Simply Cellular anti-mouse IgG beads (Bangs Laboratories), according to the manufacturer's protocol. In short, cells were grown to 90% confluency, detached with trypsin-EDTA (Gibco), and quenched using FBS-containing culture medium. 2×10^5 cells and standard beads were separately incubated with a 1:50 dilution of allophycocyanin-conjugated mouse anti-human PD-L1 antibody (BioLegend, clone MIH2) in PBSA for 1 h at 4°C with rotation. Cells and beads were then washed and analyzed on a Beckman Coulter CytoFLEX flow cytometer. MFI values of the beads were used to generate a standard curve, which was then used to extrapolate PD-L1 expression of the cells.

Receptor downregulation assays

Cells were seeded at 5×10^4 cells per well in 96 well flat bottom plates. The next day, cells were treated with 50 nM of the indicated antibody in culture medium and incubated at 37°C for various lengths of time. Cells were then washed and treated with trypsin-EDTA for 10-20 min. The trypsin was neutralized with culture medium and the cells were transferred to v-bottom plates. All subsequent steps were performed on ice. The cells were washed in PBSA and acid stripped via incubation for 30 min in 0.2 M acetic acid, 0.5 M NaCl at pH 2.0. Note that all treatments and downregulation studies were performed prior to acid solution exposure. The length of the acid strip was optimized to ensure complete removal of bound antibody. Cells were washed in PBSA and then incubated with 50 nM atezolizumab antibody for 1 h, followed by labeling with a 1:50 dilution of allophycocyanin-conjugated anti-human IgG Fc antibody (Biolegend, CloneHP6017) in PBSA. Cells were then washed and resuspended in PBSA and analyzed on a Beckman Coulter CytoFLEX flow cytometer. For monensin-based recycling studies, experiments were conducted as in the receptor down-regulation assays, except that in monensin-treated wells, 200 μM monensin sodium salt (Sigma) was added to the wells 10 min prior to antibody treatment and its presence was maintained throughout the antibody incubation period. Background-subtracted MFI values were normalized to the MFI of a control sample that was incubated in allophycocyanin-conjugated anti-human IgG Fc antibody only. Experiments were performed in triplicate or quadruplicate and conducted 3 times with similar results.

Pulse-chase assays

Antibodies were labeled using an Alexa Fluor 488 microscale labeling kit (Thermo Fisher Scientific), according to the manufacturer's instructions. Cells were seeded at 5×10^4 cells per well in 96 well flat bottom plates. The next day, the cells were treated with 50 nM Alexa Fluor 488-labeled antibody diluted in culture medium and incubated at 37°C for 2 h. Cells were then washed in culture medium and treated with 25 μg/mL anti-Alexa Fluor 488 quenching antibody diluted in culture medium (Thermo Fisher Scientific, polyclonal) at 4°C for 30 min. Cells were subsequently returned to 37°C for the indicated length of time in the continued presence of the quenching antibody. Cells were then trypsinized (Gibco) for 15 min, neutralized with FBS-containing culture medium and transferred to a v-bottom plate on ice. Cells were then washed and resuspended in PBSA and analyzed on a Beckman Coulter CytoFLEX flow cytometer.

Percent unchased signal was calculated relative to samples that were not returned to 37°C after the addition of quenching antibody for each antibody treatment condition. Experiments were performed in triplicate and conducted 2 times with similar results.

Lysosomal accumulation assays

Antibodies were labeled using the pHrodo™ iFL Green microscale labeling kit (Invitrogen P36015) according to the manufacturer's instructions. Briefly, 5×10^4 cells per well were seeded in 96 well flat bottom plates and incubated overnight. The cells were then treated with 50 nM iFL green-labeled antibody diluted in culture medium and incubated at 37°C for the given amount of time. The cells were then trypsinized (Gibco) for 15 min, neutralized with culture medium and transferred to a v-bottom plate. The cells were subsequently washed and resuspended in PBSA and analyzed on a Beckman Coulter CytoFLEX flow cytometer. Mean fluorescent intensity was normalized between treatments based on the degree of labeling. Experiments were performed in triplicate and repeated once.

Confocal microscopy

For fixed cell imaging studies, 1×10^4 cells were seeded in each well of an 8 well Nunc™ Lab-Tek™ II Chamber Slide™ System (ThermoFischer Scientific), incubated in culture medium for 2 days and then treated with 50 nM Alexa Fluor 488 labeled antibody for 12 h at 37°C. The cells were then washed once with PBS and fixed with 4% paraformaldehyde in PBS (Electron Microscopy Sciences) for 15 min at room temperature. The cells were then washed 3 times with PBS and permeabilized with 0.2% Tween20 (Sigma Aldrich) in PBS for 40 min at room temperature. The cells were washed with PBS and blocked with 1% BSA in PBS for 3 h at room temperature. The cells were then stained with 1:100 Rabbit anti-EEA1 Monoclonal Antibody (ThermoFischer Scientific MA5-14794) and 1:50 Alexa Fluor 647 Mouse Anti-Human CD107A (LAMP-1, BD Biosciences 562622) overnight at 4°C. The next day the cells were washed once with 0.02% Tween20 in PBS and twice with PBSA, and then stained with Alexa Fluor 568 Goat anti-Rabbit IgG (ThermoFischer Scientific A11011) for 1 h at room temperature. After washing 4 more times with PBS, the cells were mounted in 90% glycerol using a #1.5 glass coverslip and stored at 4°C. Fixed cell imaging was performed twice with similar results.

For live cell imaging studies, 2×10^4 cells were seeded in a #1.5 Nunc™ Lab-Tek™ II Chambered Coverglass (ThermoFischer Scientific) and incubated in culture medium for 2 days. The coverglass was then moved to the microscope and maintained at 37°C using an environmental chamber. The cells were then treated with 50 nM Alexa Fluor 647-labeled antibody in culture medium, and a series of images were taken over a 3 h time period post treatment.

All confocal microscopy was performed on a Zeiss LSM 710 NLO Inverted Confocal Microscope using a Plan-Apochromat 63X/1.4 Oil DIC lens. Image processing and analysis was performed using Fiji.[66]

Super Resolution (SR) imaging

H2444 cells were prepared on 25 mm round #1.5 coverslips and incubated with Alexa-Fluor 647-conjugated antibody for 12 h. Cells were then fixed with 4% paraformaldehyde, 0.1% glutaraldehyde in PBS for 2 h at room temperature. Samples were placed in an Attofluor cell chamber (A-7816, life technologies). The imaging buffer was prepared as follows. TN buffer consisting of 50 mM Tris and 10 mM NaCl in diH2O was prepared at pH 8.0. TNG buffer consisting of 50 mM Tris,10 mM NaCl, and 10% w/v glucose was prepared at pH 8.0. A concentrated solution of glucose oxidase and catalase was prepared as 3,376 U/mL glucose oxidase (Sigma #G2133) and 28,080 U/mL catalase (Sigma #C9332) in TN buffer, which was placed in a centrifuge at 13,000 rpm for 10 minutes. The supernatant was collected and further diluted with glycerol, yielding a final solution of 1,688 U/mL glucose oxidase, 14,040 U/mL catalase, 50% v/v TN buffer, and 50% v/v glycerol. A 1 M solution of 2-aminoethanethiol (MEA) was prepared in diH2O at pH 8.0. The imaging buffer was prepared fresh from the concentrated solutions as 168.8 U/mL glucose oxidase, 1,404 U/mL catalase, and 30 mM MEA in TNG buffer. 1.5 mL of the fresh imaging buffer was immediately placed on the sample in the Attofluor chamber and sealed with a clean 25 mm round #2 coverslip. The sealed Attofluor chamber was placed at room temperature for 30 minutes to allow the oxygen scavenging reaction to progress before imaging. Direct stochastic optical reconstruction microscopy (dSTORM) imaging was performed using a custom-built microscope equipped with a 1.35 NA silicon oil immersion lens (UPLSAPO100XS, Olympus) and an sCMOS camera (C11440-22CU, Hamamatsu). A 647 nm fiber laser (2RU-VFL-P-500-647-B1R, MPB Communications) was used for excitation light. Emission light was collected with a 708/75 nm band pass filter (FF01-708/75-25, Semrock). Brightfield registration[67] was performed before each sequence using a 660 nm LED (M660L3, Thorlabs) illumination lamp and a 3D piezo sample stage (MAX341/M, Thorlabs). A total of 60,000 frames were collected for each cell (10 sequences of 6,000 frames each) at 100 frames per second.

Super Resolution (SR) image analysis

Raw dSTORM data were processed as follows.[68] Emitter candidate locations were found by applying a difference of Gaussians filter to images and identifying local maxima. Subregions were drawn around local maxima and emitter photon counts were estimated assuming each subregion contains a single emitter. Subregions containing candidates with photon counts above a threshold were retained. A Gaussian point spread function (PSF) model was used to fit candidate emitters as described previously,[69] assuming one emitter per subregion. Resulting localizations were thresholded based on their estimated photons, background, Cramér-Rao lower bound of the fit coordinates, and a p-value describing the goodness of fit of the PSF model. A frame-connection algorithm[70] was applied to the retained localizations to combine localizations arising from a single blinking event of an emitter, followed by a final drift-correction[67] algorithm to correct for residual sample drift.

Cluster analysis

The four SR images for each of the two datasets were broken up into four ROIs per image covering the entire image, producing a total of 16 128x128 pixel ROIs per dataset. The SR localizations in each of these ROIs was analyzed using DBSCAN,[71] setting the parameters epsilon (the minimum distance between separate clusters of points, or equivalently, the maximum nearest neighbor distance between points within a cluster) to 100 nm, and the minimum number of points for a point ensemble to be considered a cluster (N) to 10. These values were chosen after a parameter study varying epsilon and N, and assessing the clustering produced. The data was collected and analyzed for the total clustered fraction of localizations per ROI. The observed trends were observed consistently over a wide range of DBSCAN parameters. The clustered fraction per ROI in the two datasets was then compared by performing a two-sample Kolmogorov-Smirnov goodness-of-fit hypothesis test[72] using the MATLAB function kstest2. The P-value produced indicated the likelihood that the null hypothesis that the two data collections come from the same distribution would not be rejected. All these analyses were done in MATLAB.

Cell surface binding studies

PD-L1-expressing CHO-K1 cells were grown to 90% confluency, detached with trypsin-EDTA (Gibco), quenched using FBS-containing culture medium, resuspended in PBSA, and aliquoted into a 96-well plate a 1×10^5 cells per well. Cells were then incubated with various concentrations of either atezolizumab or TS1521 diluted in PBSA for 2 h at 4°C. Cells were subsequently washed and incubated with a 1:50 dilution of allophycocyanin-conjugated anti-human IgG Fc antibody (Biolegend, CloneHP6017) in PBSA. Cells were washed, resuspended in PBSA, and analyzed on a Beckman Coulter CytoFLEX flow cytometer. Data were analyzed in Prism software (GraphPad) using a single logistic model, and equilibrium dissociation constant (K_D) values were determined. Experiments were performed in triplicate and repeated twice with similar results.

PD-1/PD-L1 blockade TCR activation reporter cell assay

A PD-1/PD-L1 Blockade Bioassay kit was obtained from Promega, containing Bio-Glo luciferase substrate and 2 cell lines: CHO-K1 cells expressing PD-L1 and a T-cell-activating surface protein (antigen-presenting cells, APCs); and Jurkat T cells expressing PD-1 and cognate TCR driving a luciferase reporter via a nuclear factor of activated T-cells (NFAT) response element (effector cells). The assay was performed according to the manufacturer's protocol, with slight modifications noted below.

5×10^4 APCs were plated in each of the innermost 60 wells of two 96-well, opaque white, flat-bottom plates at a density of 500,000/mL, while the peripheral wells were filled with an identical volume of cell medium. Assay plates were then incubated overnight (16-20 h) at 37°C, after which the medium was aspirated. Serial dilutions of antibody were prepared in assay buffer (RPMI medium supplemented with 1% FBS). For samples wherein the antibody was removed prior to effector cell addition (hereafter called wash plate), 40 μL of diluted antibody was added to each well of APCs, followed by 40 μL of assay buffer. For samples wherein the antibody was not removed (hereafter called control plate), 80 μL of assay buffer was added to each well of APCs in two, 40 μL increments. Both plates were then returned to the incubator for 2 h at 37°C. A 10 mL solution of effector cells was prepared to a density of 1.25 million cells/mL in assay buffer. After the 2-h incubation period, both plates had their innermost 60 wells again aspirated of volume. To the wash plate, 40 μL of antibody serial dilution was added to each well followed by 40 μL of effector cells. To the control plate, 40 μL of assay buffer was added to each well, followed by 40 μL of effector cells. Both plates were then returned to the incubator for 6h at 37°C. The plates were then removed from the incubator and equilibrated to ambient temperature for 10 min in the dark. 80 μL of Bio-Glo reagent was added to each well. The plates were incubated in darkness for 10 min and luminescence was read on a BioTek Synergy 2 Multi-Mode Microplate Reader. Data was normalized to a cell-free control, and half-maximal effective concentration (EC_{50}) was determined by fitting to a single logistic model using Prism software (GraphPad).

ELISpot T-Cell Activation Assay

Peripheral blood mononuclear cells (PBMCs) from subjects enrolled in the BBAASH cohort as previously described,[53] and who became chronically infected with HCV were thawed from time points wherein HCV-specific T-cell responses were previously shown to induce high PD-1 levels.[73] All specimens were tested that contained sufficient cell numbers for analysis, and the wash conditions were only tested on donor 175 due to limited cell numbers for donor 29. The ability for T cells to produce interferon-gamma (IFN-γ) in response to HCV peptides after incubation with anti-PDL1 antibodies was measured by IFN-γ enzyme-linked immunosorbent spot (ELISpot), as described previously,[74,75] with modifications. 96-well polyvinylidene plates (Millipore) were coated with 5μg/ml recombinant human anti-IFN-γ antibody (MAbtech clone 1-D1K) in PBS at 4°C overnight. Previously frozen PBMCs were incubated with 10nM TS1521 or Atezolizumab in R10 media (RPMI 1640, 10% FBS, and 10 mM Hepes buffer with 2mM glutamine and antibiotics [50 U/ml penicillin-streptomycin]) for one hour prior to stimulation with HCV peptides. Following incubation, 50% of the cells were washed and then given fresh R10 media to remove the soluble anti-PD-L1 antibodies. PBMCs were plated at 200,000 cells/well in 50μL R10 media on the streptavidin-coated polyvinylidene plates. HCV peptides were added directly to the wells at a final concentration of 0.02 μg/mL. The plates were incubated at 37°C, 5% CO2 for 20 hours. Plates were then washed and incubated with 0.5 μg/mL biotin-labeled anti-IFN-γ antibody (MAbTech clone 7-B6-1) in PBS containing 0.5% BSA. Plates were developed as previously described.[74] Spots (corresponding to IFN-γ-secreting cells) were counted by the Immunology Core at Johns Hopkins University. ELISpot assays for each subject were performed twice. A positive immune response was defined as more than 48 spot-forming cells per 1,000,000 PBMCs.[74]

Mouse pharmacokinetic and biodistribution studies

All mouse studies were conducted under Johns Hopkins University Animal Care and Use Committee approved protocols. NSG mice were obtained from the Johns Hopkins University Immune Compromised Animal Core. For both studies, mice were implanted with tumor cells approximately two weeks prior to dosing.

For pharmacokinetic studies, 6 week-old female NSG mice (n=4 mice per cohort) were implanted orthotopically with 2.5×10^6 MDA-MB-231 cells. Antibody labeled with IRDye 800CW NHS Ester (Li-Cor) was mixed 1:4 with unlabeled antibody, and 10 mg/kg total antibody was injected intravenously at a concentration of 2.5 mg/mL in PBS. Images were taken using a Li-Cor Pearl Impulse Imager. Quantitation of tumor localization based on fluorescent intensity was analyzed using Pearl Impulse Software and plotted in GraphPad Prism.

For biodistribution studies, 6 week-old female NSG mice (n=5 mice per cohort) were implanted orthotopically with 2.5×10^6 MDA-MB-231 cells. On day 16 after tumor implantation, mice in the 96 h treatment group were injected intravenously with either 1 mg/kg antibody in PBS at a concentration of 0.1 mg/mL. On day 19, mice in the 24 h treatment group were given an identical dose. On day 20, all mice were injected intravenously with 30 μCi of [^{18}F]DK222 and tissues were harvested, including blood, muscle, tumor, heart, lung, liver, spleen, and kidney. Harvested tissues were weighed and analyzed in an automated gamma counter (Perkin Elmer - 2480 Automatic Gamma counter - Wizard2 3'' Wallac, Waltham, MA), and the percentage of incubated dose per gram of tissue (%ID/g) values were calculated as described previously.[54]

QUANTIFICATION AND STATISTICAL ANALYSIS

All statistical analyses were performed using GraphPad Prism software (v9.3.1). The sample size, number of cell replicates, number of mice, definition of center, dispersion and precision measures, and type of analyses performed are described in the above section where applicable. Statistical significance is defined as $p<0.05$ (*$p<0.05$; **$p<0.01$; ***$p<0.001$; ****$p<0.0001$). Significance between all groups is not always shown in figures. For full analyses see Table S4.

Update

Cell Chemical Biology
Volume 31, Issue 5, 16 May 2024, Page 1023

DOI: https://doi.org/10.1016/j.chembiol.2024.04.011

Cell Chemical Biology

Correction

Multiparatopic antibodies induce targeted downregulation of programmed death-ligand 1

Seth D. Ludwig, Bunyarit Meksiriporn, Jiacheng Tan, Rakeeb Kureshi, Akhilesh Mishra, Kyle J. Kaeo, Angela Zhu, Georgia Stavrakis, Stephen J. Lee, David J. Schodt, Michael J. Wester, Dhiraj Kumar, Keith A. Lidke, Andrea L. Cox, Helen M. Dooley, Sridhar Nimmagadda, and Jamie B. Spangler*
*Correspondence: jamie.spangler@jhu.edu
https://doi.org/10.1016/j.chembiol.2024.04.011

(Cell Chemical Biology *31*, 904–919.e1–e11; May 16, 2024)
In the originally published version of this article, Dhiraj Kumar was not listed as an author. This has now been corrected both online and in print. The authors regret this error and apologize for any confusion that it has caused.

 © 2024 Elsevier Ltd. All rights reserved.